Journal of Materials Chemistry C

ROYAL SOCIETY OF CHEMISTRY

PAPER

View Article Online
View Journal | View Issue

Cite this: J. Mater. Chem. C, 2023, 11, 8129

Thermal quenching of lanthanide luminescence *via* charge transfer states in inorganic materials

Pieter Dorenbos

There are various routes of luminescence quenching such as multi-phonon relaxation from excited states to lower energy states, energy migration to killer sites, and radiation less relaxation to the ground state via the crossing point in a configurational coordinate diagram. In this work, we will consider and review quenching of lanthanide luminescence by means of charge carrier transfer to the valence band or the conduction band of the host compound. We will focus on $4f^n$–$4f^n$ emission quenching due to thermally activated electron transfer from the Pr^{3+} $^3P_0$ level and the Tb^{3+} $^5D_4$ level to the conduction band, and due to thermally activated hole transfer from the Eu^{3+} $^5D_0$ level to the valence band. In addition, we will consider the quenching of the $4f^{n-1}5d$–$4f^n$ emission of Eu^{2+} and Ce^{3+} which often (if not always) proceeds by electron transfer to the conduction band. Since all the above quenching routes involve reduction or oxidation of lanthanides, the location of the lanthanide charge transition levels with respect to the host bands is crucial. In other words, we need to know the location of the ground and excited states in the band gap or equivalently the vacuum referred binding energies (VRBE) in the lanthanide states as can be established using the (refined) chemical shift model. A clear correlation between the temperature T_{50} at which luminescence intensity or luminescence decay time has dropped by 50% and thermal quenching activation energies ΔE derived from VRBE schemes will be demonstrated. Since T_{50} typically changes 400–800 K with a 1 eV change in ΔE, and since VRBE energies may contain 0.3–0.5 eV error, it will be clear that the accurate prediction of quenching temperatures from the VRBE data is not yet feasible. Nevertheless, one may derive trends and provide guidelines on how to improve the thermal stability of luminescence.

Received 19th October 2022,
Accepted 1st December 2022

DOI: 10.1039/d2tc04439k

rsc.li/materials-c

Anniversary statement

Ten years ago, the J. Mater. Chem. C was a 'new kid on the block' in our field of luminescence phosphors. It has evolved quite rapidly into a high impact factor journal publishing manuscripts related to luminescence materials and their application in devices. We together with collaborating groups have almost yearly published manuscripts in JMCC on topics such as thermal quenching in Ce doped garnets, persistent luminescence, carrier dynamics and trapping in phosphors, computational studies on the spectroscopy of lanthanides, and conduction and valence band engineering of phosphor properties. The high impact factor is reflected in the frequency of citations to our work.

1 Introduction and theory

The thermal quenching of luminescence is an important phosphor characteristic for many different applications. For application at room temperature, the onset for thermal quenching should obviously be well above 300 K. Luminescent phosphors in modern day light emitting diode (LED) lighting like Ce^{3+} doped garnet $Y_3Al_5O_{12}$ typically operate at temperatures around 100 C,[1] and phosphors should not start to quench then. High power white light emitting (WLED) phosphors require thermal stability up to at least 200 C (475 K).[1,2] The thermal quenching of emission intensity or emission decay time is also used in thermometry.[3–5] Thermal barrier coating phosphors (TBCs) are used to sense the temperature in turbine engines up to temperatures as high as 1200 K, see, *e.g.*, ref. 6 and 7. Understanding how the quenching temperature depends on the type of the luminescence activator and the type of host compound is then important for research and development, or even for engineering of new phosphor materials towards a specific application. Luminescence intensity can be decreased by various quenching mechanisms as illustrated in Fig. 1 where a luminescence center with a ground state (g.s.) and several

Delft University of Technology, Faculty of Applied Sciences, Department of Radiation Science and Technology, Mekelweg 15, 2629 JB Delft, The Netherlands. E-mail: p.dorenbos@tudelft.nl; Tel: +31 15 2781336

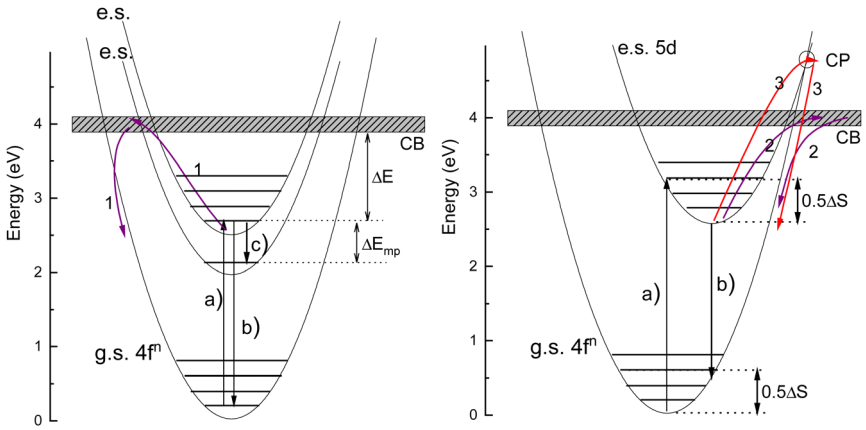

Fig. 1 Illustration of the various quenching mechanisms in lanthanide luminescence. Arrows (1)–(3) in the two configurational coordinate diagrams illustrate the quenching of $4f^n$ emission via the conduction band (CB), quenching of 5d emission via the CB, and quenching of 5d emission *via* the crossing point (CP), respectively. Arrow (c) in the left hand panel illustrates the quenching of 4f–4f emissions via multi-phonon relaxation to a ΔE_{mp} lower lying excited state. The contributions to the Stokes shift ΔS from the excited and ground state relaxation for 5d–4f emissions are indicated in the right hand panel. The Stokes shift is negligible for 4f–4f transitions in the left hand panel.

excited states (e.s.) is shown. Quantum efficiency is 100% when each absorbed photon via transition (a) results in an emitted photon via *e.g.* transition (b). However, the system can also decay to a lower lying level by means of the emission of multiple phonons indicated by transition (c) in the left panel. The rate will depend on the available phonon energies, the temperature, and the energy that needs to be bridged. Energy transfer to a nearby defect is also a well-known route of luminescence quenching. In this work, we will focus on the thermally activated quenching of lanthanide luminescence under conditions where multi-phonon relaxation and energy transfer are improbable. In practice, this means that the activator and defect concentrations should be smaller than typically 1% and that the energy gap ΔE_{mp} between the emitting level and the next lower level should be larger than typically 1 eV.

Fig. 2 shows the relevant $4f^n$ levels of lanthanides Pr^{3+} ($n = 2$), Eu^{3+} ($n = 6$), and Tb^{3+} ($n = 8$). We will consider the thermal quenching of the luminescence from the $^3P_0$ level of Pr^{3+}, the $^5D_0$ level of Eu^{3+}, and the $^5D_4$ level of Tb^{3+}. Here, the energy gaps ΔE_{mp} with the next lower $^1D_2$, $^7F_6$, and $^7F_0$ 4f levels are 0.5 eV, 1.55 eV, and 1.82 eV, respectively. Whenever the $^5D_4$ or $^3P_0$ level is close to the CB-bottom, quenching may proceed via the charge transfer state. This means that an electron is thermally excited from the emitting $4f^n$ excited state to the conduction band (CB) of the host compound as illustrated with arrows (1) in Fig. 1. The energy difference ΔE between the location of the emitting state in the band gap and the CB-bottom is then the relevant quenching energy barrier. In the case of Pr^{3+}, there is only 0.5 eV energy difference with the next lower $4f^2$ state and the quenching route via multi-phonon relaxation to $^1D_2$ also need to be considered. Charge transfer quenching also applies to Eu^{3+}, but instead of electron ionization to the CB quenching proceeds by hole ionization to the valence band (VB), *i.e.*, Eu^{3+} ($^5D_0$) → Eu^{2+} ($^8S_{7/2}$) + VB_h where a valence band hole (VB_h) is created.

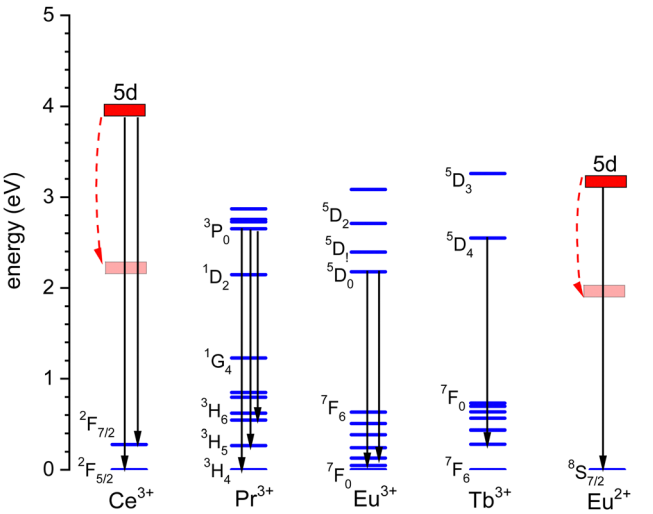

Fig. 2 Relevant level energies and luminescence transitions of Ce^{3+}, Pr^{3+}, Eu^{3+}, Tb^{3+}, and Eu^{2+}. The energy of the lowest 5d-level depends on the compound and the range is indicated by the curved dashed arrows.

Ce^{3+} and Eu^{2+} show the dipole allowed $4f^{n-1}$ and $5d–4f^n$ emissions. Different from exciting a $4f^n$ state there will be significant lattice relaxation after exciting to a $4f^{n-1}5d$-state. This leads to an offset in the configuration coordinate diagram as illustrated in Fig. 1. Thermal quenching may proceed *via* either electron ionizations to the CB illustrated by arrows (2) or alternatively when the CB is above the crossing point (CP) in the configurational coordinate diagram *via* that CP as illustrated by arrows (3) in Fig. 1.

In this work, we will focus on the quenching route *via* charge transfer to either the CB or the VB, and then the level locations of the emitting levels in the band gap need to be known in order to determine the quenching energy barrier ΔE. These level locations will be established with the (refined) chemical shift model developed in 2012 (and 2019).[8–10] It makes use of

the highly systematic changes in the level location with the number n of electrons in the $4f^n$-orbital of the lanthanides which is then combined with the spectroscopic data retrieved from the archival literature. It provides the so-called vacuum referred binding energy (VRBE) diagrams where all divalent and trivalent lanthanide ground and excited state levels are drawn with respect to the VB-top and CB-bottom and also with respect to the vacuum level. This work deals with about 170 different inorganic compounds, and for each compound the available spectroscopic data on the host and on divalent and trivalent lanthanides were gathered and combined to construct their VRBE diagrams. It is not doable to provide the references and analysis for each piece of data used (it would run into many 1000), and the reader has to trust that everything was performed with best scientific effort. Many VRBE schemes have already appeared in the literature where many references to the original data can be found. The reader may also conduct own search in the archival literature to derive, verify or improve the parameters used. The relevant parameters in the VRBE construction will be tabulated for each host and only the reference to information on the thermal quenching data will be provided.

A. Arrhenius equation, the chemical shift model and the VRBE scheme

The thermal quenching of luminescence intensity $I(T)$ is traditionally expressed using the single barrier Arrhenius equation

$$I(T) = \frac{I(0)}{1 + \frac{\Gamma_0}{\Gamma_\nu}\exp\left(\frac{-\Delta E}{k_B T}\right)} \quad (1)$$

where Γ_ν is the radiative decay rate, Γ_0 is the attempt rate for thermal quenching which has similar magnitude as the maximum phonon frequency in compounds, k_B is the Boltzmann constant, and ΔE is the energy barrier for thermal quenching.

A similar equation applies for the lifetime $\tau(T)$ of the excited state

$$\tau(T) = \frac{\tau_\nu}{1 + \frac{\Gamma_0}{\Gamma_\nu}\exp\left(\frac{-\Delta E}{k_B T}\right)} = \frac{I(T)}{I(0)}\tau_\nu \quad (2)$$

where τ_ν is equivalent to $1/\Gamma_\nu$.

Depending on whether defects or dislocations happen to be nearby the activator or not, ΔE may change from activator to activator and therefore become spatial dependent. In cases where quenching proceeds by electron transfer to the CB or hole transfer to the VB, ΔE will also show a temperature dependence because the bandgap of the host compound will be temperature dependent. Due to lattice expansion when the temperature increases the (mobility) bandgap reduces typically by 0.05 eV per 100 K temperature increase. Therefore, the often made assumption of a temperature independent and a single value ΔE fails largely in practice. Furthermore, the radiative decay time usually shows a temperature dependence, *i.e.*, it tends to increase with the temperature increase, see *e.g.* the quenching curves in ref. 11. Considering all the above, a single barrier Arrhenius fit to an experimental quenching curve will not provide good parameters for the activation energy and frequency factor. Instead of fitting, we will use a fixed value for Γ_0 and estimate the average quenching energy barrier ΔE from the temperature where the luminescence intensity or decay has decreased by 10% (T_{10}) or 50% (T_{50}).

Using eqn (1) and (2), one obtains

$$T_{50} = \frac{11\,600}{\ln(\tau_\nu \Gamma_0)}\Delta E \quad (3)$$

and

$$T_{10} = \frac{11\,600}{\ln 9 + \ln(\tau_\nu \Gamma_0)}\Delta E \quad (4)$$

where Γ_0 depends on the type of compound and ranges from 4×10^{12} Hz for iodide compounds with weakly bonded heavy ions up to 4×10^{13} Hz for strongly bonded borate and phosphate compounds.[12] This corresponds with phonon energies ranging from 130 cm^{-1} to 1300 cm^{-1}. In this work, we adopt the same typical value of $\Gamma_0 = 2 \times 10^{13}$ Hz for each compound. For each lanthanide (*A*), we adopted a typical decay time τ_ν as listed in Table 1. The nature of the transitions and their typical emission wavelengths λ are also compiled in Table 1. Those for Tb^{3+}, Pr^{3+}, and Eu^{3+} are almost independent of the type of compound but those for the 5d–4f emissions of Eu^{2+} and Ce^{3+} depend strongly as illustrated in Fig. 2. Since the product $\tau_\nu\Gamma_0$ appears as an argument in the natural logarithm of eqn (3), a factor 4 error in $\tau_\nu\Gamma_0$ will lead to only 5% error in T_{50}. The dependences of T_{50} and T_{10} on ΔE in columns 5 and 6 are obtained using eqn (3) and (4). The ratio, or the slope in K eV^{-1}, increases with a shorter decay time of the luminescence.

B. Chemical shift model with the characteristic VRBE diagram

Fig. 3 shows the vacuum referred binding energy diagram for the lanthanides in YPO_4 as constructed using the (Refined) Chemical Shift model. The model was first introduced in 2012[8] and refined later in 2019.[9,10] The diagram shows the location of the divalent and trivalent ground states within the band gap and relative to the vacuum level. The vacuum referred binding energies are equivalent to the $Ln^{3+/2+}$ and $Ln^{4+/3+}$ charge transition levels. The most crucial parameter needed to construct a VRBE scheme is the *U*-value defined as the energy difference between the $Eu^{3+/2+}$ and $Eu^{4+/3+}$ CTLs which was determined as 7.09 eV for YPO_4. The chemical shift model relates the *U*-value

Table 1 The dependences of T_{50} and T_{10} on the activation energy ΔE calculated for $\Gamma_0 = 2 \times 10^{13}$ Hz and using the typical value for τ_ν in column 4

A	Transition	λ (nm)	τ_ν	$T_{50}/\Delta E$ (K eV^{-1})	$T_{10}/\Delta E$ (K eV^{-1})
Eu^{3+}	$^5D_0 \rightarrow {}^7F_{1,2}$	≈610	2 ms	475	435
Tb^{3+}	$^5D_4 \rightarrow {}^7F_5$	≈545	2 ms	475	435
Pr^{3+}	$^3P_0 \rightarrow {}^3H_{4,5,6}$	490, 550, 620	50 μs	560	510
Eu^{2+}	$5d \rightarrow 4f[^8S_{7/2}]$	380–600	1000 ns	690	610
Ce^{3+}	$5d \rightarrow 4f[^2F_{5/2,7/2}]$	300–550	40 ns	850	735

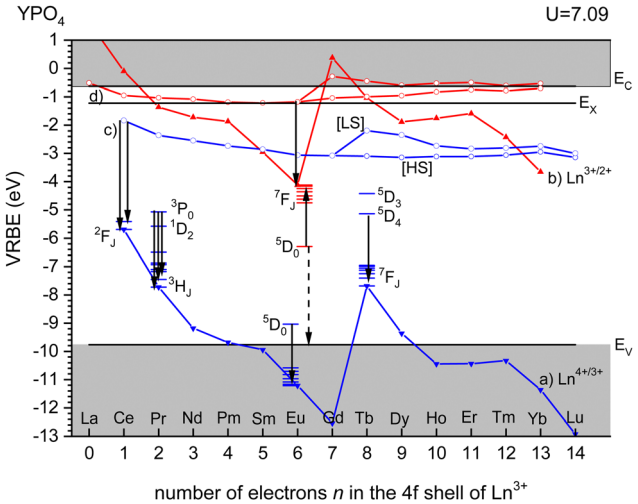

Fig. 3 Vacuum referred binding energy scheme for the trivalent and divalent $4f^n$ lanthanide ground state levels in YPO_4. (a) Connects the VRBE in the Ln^{3+} $4f^n$ ground state levels and can also be denoted as the $Ln^{4+/3+}$ charge transition levels. (b) Connects the same for divalent lanthanides. (c) Connects the VRBE in the lowest energy $4f^{n-1}5d$ states of trivalent lanthanides where for $n > 7$ a distinction between the high spin [HS] and the low spin [LS] states is made. (d) Connects the same for divalent lanthanides. E_V, E_X, and E_C are the VRBE at the valence band top, in the host exciton state, and at the conduction band bottom, respectively.

with the VRBEs of the $Eu^{3+/2+}$ and $Eu^{4+/3+}$ CTLs.[8] The second parameter is the energy E^{CT} for electron transfer from the valence band top to Eu^{3+} which when subtracted from the $Eu^{3+/2+}$ CTL defines the VRBE E_V at the VB-top. The third parameter is the energy E^{ex} for the host exciton creation where we will always use the (estimated) value that pertains to a low temperature ($\approx$10 K). When added to E_V, it defines the VRBE E_X of the electron in the exciton state. Bandgaps and exciton energies typically increase 0.05 eV at 100 K temperature lowering which means that a correction of about 0.15 eV is needed from the room temperature value. Finally, one needs to add the exciton electron hole binding energy E_{eh} to E_X in order to reach the VRBE E_C at the bottom of the CB. As a rule of thumb, we used $E_{eh} = 0.008(E^{ex})^2$ as proposed in ref. 13. The CTLs for lanthanides other than Eu^{2+} and Eu^{3+} are then obtained by using the systematics in the shapes of the CTL curves (zig-zag curves) as treated in the Refined Chemical Shift model.[9,10] The Dieke diagrams for the divalent and trivalent lanthanides are then used to determine the VRBE in the excited lanthanide states.

Fig. 3 shows the $4f^2$, $4f^6$, and $4f^8$ level locations of Pr^{3+}, Eu^{3+}, and Tb^{3+} together with the $4f^n$–$4f^n$ luminescence transitions of relevance to this work indicated by the arrows. In the case of Eu^{3+}, the levels and transition are shown with both the usual 'electron picture' and the less familiar 'hole-picture'.[14] The scheme shows that the lowest Eu^{2+} 5d state is close below the CB-bottom. The emitting 5d-state for Ce^{3+} is always further below. Note that the energy gap ΔE_{mp} to the $^2F_{7/2}$ level for Ce^{3+} and to the ground state of Eu^{2+} is several eV and multi-phonon relaxation is highly improbable. It is already well-established that the thermal quenching of these lanthanides usually proceeds by thermally activated electron transfer from the 5d-state to the conduction band, see Fig. 1.

For YPO_4, the emitting $^3P_0$ level of Pr^{3+} and the $^5D_4$ level of Tb^{3+} appear at mid band gap near -5 eV VRBE. The energy difference with the CB-bottom is very large (>4 eV) and the thermal quenching of these emissions in YPO_4 proceeds by other routes than *via* the CB. However, in compounds where the CB is located below, say, $E_C = -3$ eV thermal quenching *via* the conduction band becomes important. Thermal ionization to the CB from the $^5D_0$ level of Eu^{3+} will be impossible for all types of compounds. Instead, quenching takes place *via* the VB $\rightarrow$ Eu^{3+} charge transfer state which can be best visualized with the 'hole picture'.[14] Here, the ground state of Eu^{3+} is visualized as a hole trapped by Eu^{2+} which is then placed at the $Eu^{3+/2+}$ CTL. Excitation of Eu^{3+} implies that the hole is excited downwards in the VRBE scheme. Thermal quenching can now proceed by ionization of the hole to the valence band illustrated by the dashed arrow. The quenching energy barrier ΔE is then the energy difference between the $^5D_0$ level and E_V.

II. Results

A. Thermal quenching of the Eu^{3+} $^5D_0$ emission

Even at 1000 K, it is unlikely that the $^5D_0 \rightarrow {}^7F_J$ luminescence transitions of Eu^{3+} will be quenched by multi-phonon relaxation. The energy difference of 1.55 eV with the next lower energy $^7F_6$ level is just too large to bridge. Instead, quenching proceeds *via* the VB $\rightarrow$ Eu^{3+} charge transfer state. This implies that the excitation energy of the $^5D_0$ level of about 2.18 eV together with the energy supplied from the thermal bath is converted into a state with a hole in the VB together with Eu^{2+} in its ground state. In the VRBE scheme, this is illustrated with the 'hole picture' where the $^5D_0$ state is located 2.18 eV below the $Eu^{3+/2+}$ CTL. Since the $Eu^{3+/2+}$ CTL appears always near -4 eV, the quenching temperature will be directly linked to the VRBE E_V at the VB-top, and one needs to lower the VB to increase thermal stability. The energies E^{CT} at the maximum of the Eu^{3+} CT-band observed in the excitation spectra of the Eu^{3+} emission for several hundred different compounds were compiled in 2005.[15] Since 2005, many more data or more accurate data have appeared and the values reported in the Tables to follow provide the, in the authors' opinion, most likely values.

A relationship between the Eu^{3+} luminescence quantum efficiency at room temperature and the energy E^{CT} was established long time ago by Blasse.[16] Later, Struck and Fonger[17] studied the quenching as a function of temperature and explained it in terms of a configurational coordinate diagram involving the charge transfer state. In ref. 18, the data compiled on 12 different compounds revealed a linear relationship between E^{CT} and T_{10} in a 0 to 800 K temperature range. Later, in ref. 13, 13 more compounds were added to the compilation. In ref. 14, the 'hole picture' was used to describe the quenching by hole ionization and a $T_{10}/\Delta E$ of $\approx$ 430 K eV^{-1} relationship

was found which agrees well with the prediction from eqn (4) as listed in Table 1.

In this work, we added new information. We selected compounds with a relatively low Eu^{3+} concentration (about 1%). Often, the data for decay time quenching were preferred over those of intensity quenching because the latter tend to be less accurate. The results are shown in Fig. 4 and the data and references are found in Table 2. We also added information on E^{ex} and the U-values from which the data on E_V and E_C are obtained using the refined chemical shift model. The typical error bars are ±0.12 eV in the CT-energy and ±50 K in the T_{10} value. ΔE on the horizontal axis was obtained by

$$\Delta E = E^{CT} - E(^5D_0) - 5 \times 10^{-5} T_{10} E^{ex} \quad (5)$$

where $5 \times 10^{-5} T_{10} E^{ex}$ is the estimated lowering of the bandgap at a temperature T_{10} where we assumed that the amount of lowering scales with E^{ex}. This is motivated as follows. The VRBE of cation electrons lowers (becomes more negative) when neighboring anions move further away; this is simply a matter of less Coulombic repulsion from the negatively charged anions. The VRBE of anion electrons raises (becomes less negative) when neighboring cations move further away; this is a matter of decreased Coulombic attraction from the positively charged cations. As a result, the cation related CB-bottom moves down and the anion related VB-top moves up causing the bandgap to decrease. For Eu^{2+}, being a cation, we will assume that its VRBE lowers with the same pace as the CB-bottom. Since the VB-top moves upwards, ΔE will decrease with the same amount as the bandgap lowering.

There are few outliers notably $ScBO_3$, $ScPO_4$ and YVO_4 as shown in Fig. 4. Disregarding these, a linear least square fit through the data yields the dashed line with a slope of 421 K eV^{-1} which agrees very good with a predicted value of 435 K eV^{-1} as shown in Table 1. The compound to compound variation in decay time, in maximum phonon frequencies, and in relaxation effects, and the experimental errors in E^{CT} and T_{10} then provide the scatter of data.

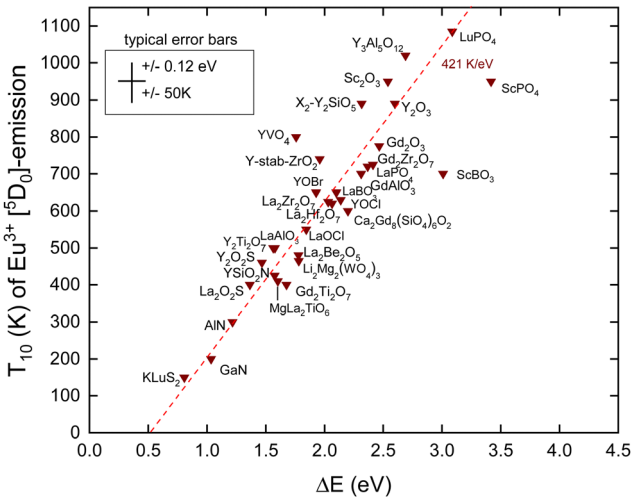

Fig. 4 10% Quenching temperature T_{10} for the Eu^{3+} emission from the $^5D_0$ level against the energy difference between the $^5D_0$ hole state and the VB-top. The fitted dashed line has a slope of 421 K eV^{-1}.

Table 2 Data on T_{10} values for the Eu^{3+} $^5D_0$ emission and the quenching energy barriers ΔE derived from E^{CT} and E^{ex} energies. The parameters used for the VRBE-diagram construction are provided. All energies are in eV

A	U	E^{CT}	E_V	E^{ex}	E_C	ΔE	T_{10}	Ref.
LaOCl	6.65	4.20	−8.10	6.45	−1.32	1.85	550	19
YOCl	6.65	4.54	−8.44	7.10	−0.94	2.14	630	20
YOBr	6.57	4.32	−8.18	6.50	−1.34	1.93	650	20
$LaPO_4$	7.18	4.84	−9.00	8.10	−0.38	2.37	720	7
$LuPO_4$	7.08	5.74	−9.85	8.70	−0.55	3.09	1085	7,21
$ScPO_4$	7.02	5.95	−10.0	7.40	−2.19	3.42	950	7,22
$LaBO_3$	6.93	4.51	−8.54	7.05	−1.10	2.10	650	23,24
$ScBO_3$	6.86	5.44	−9.44	7.10	−1.94	3.01	700	24
$Ca_2Gd_8(SiO_4)_6O_2$	6.80	4.59	−8.56	7.00	−1.17	2.20	600	7
X2-Y_2SiO_5:(Ce1)	6.86	4.80	−8.80	6.82	−1.61	2.32	890	7,25
$LaAlO_3$	6.76	3.91	−7.86	6.10	−1.47	1.58	500	26
$GdAlO_3$	6.75	4.75	−8.70	7.36	−0.90	2.31	700	4
$Y_3Al_5O_{12}$	6.77	5.23	−9.19	7.10	−1.69	2.69	1020	7
$Li_2Mg_2(WO_4)_3$	7.15	4.07	−8.21	4.70	−3.34	1.78	465	27
YVO_4	6.80	4.10	−8.07	4.00	−3.94	1.76	800	7
$MgLa_2TiO_6$	6.68	3.88	−7.79	4.50	−3.13	1.60	410	28
$Gd_2Ti_2O_7$	6.79	3.94	−7.91	4.15	−3.62	1.68	400	29
$Y_2Ti_2O_7$	6.79	3.85	−7.82	4.25	−3.42	1.56	500	2
$Zr_{0.83}Y_{0.17}O_{1.91}$	6.70	4.34	−8.26	5.40	−2.63	1.96	740	7,30
$La_2Zr_2O_7$	6.66	4.43	−8.33	6.00	−2.05	2.06	620	5,31
$La_2Hf_2O_7$	6.65	4.40	−8.30	6.00	−2.01	2.03	625	5,31
$La_2Be_2O_5$	6.70	4.11	−8.03	6.28	−1.44	1.78	480	32
$Gd_2Zr_2O_7$	6.65	4.81	−8.71	6.00	−2.42	2.41	725	6
C-Gd_2O_3:(S_6)	6.60	4.86	−8.74	5.50	−2.99	2.47	775	33
C-Y_2O_3:(S_6)	6.60	5.05	−8.93	6.10	−2.53	2.60	890	33,34
C-Sc_2O_3:(C_2)	6.60	5.02	−8.90	6.30	−2.28	2.54	950	33
La_2O_2S	6.37	3.64	−7.41	4.75	−2.48	1.37	400	19,35
Y_2O_2S	6.37	3.76	−7.53	4.85	−2.49	1.47	460	19
$KLuS_2$	6.20	3.02	−6.71	4.35	−2.21	0.81	150	36
$YSiO_2N$	6.70	3.89	−7.81	6.10	−1.41	1.58	425	37
AlN-wurtzite	6.40	3.49	−7.27	6.20	−0.76	1.22	300	38
GaN-wurtzite	6.40	3.25	−7.03	3.48	−3.45	1.04	200	38–40

Note that the fitted line does not cross the horizontal at zero energy but near 0.5 eV. We assumed that quenching occurs by the full ionization of the hole. However, this is not necessarily needed. The CT-state is a hole at the valence band that is still Coulomb bonded with the transferred electron, *i.e.*, Eu^{2+}, and radiation less recombination may start from this bonded state which will lower ΔE. Furthermore, 0.5 eV is of the same magnitude as the energy involved in lattice relaxation and Stokes shift.[15,41] We therefore interpret the intercept near 0.5 eV as an effect of electron–hole bonding and lattice relaxation.

B. Thermal quenching of the Tb^{3+} $^5D_4$ emission

The energy gap between the emitting $^5D_4$ level of Tb^{3+} and the next lower $^7F_0$ $4f^8$-level is about 1.8 eV. This is even larger than that in the case of Eu^{3+} considered above, and multi-phonon relaxation is like for Eu^{3+} not a feasible quenching mechanism. Instead, in cases where the CB-bottom is not too far above the $^5D_4$ level, thermal quenching can proceed by electron ionization to the CB. For YPO_4 in Fig. 3 with the CB-bottom at −0.63 eV, the distance is 4.5 eV which is clearly too large. However, in transition metal based compounds like tantalates, tungstates, vanadates, niobates, molybdates and titanates, the CB-bottom appears at −3 eV to −4 eV.[42] The excitation spectra

of the Tb^{3+} emission in these compounds often reveal a so-called intervalence charge transfer (IVCT) band attributed to the excitation of an electron from the Tb^{3+} $^7F_6$ ground state[43,44] to the CB. Whereas the CT-band energy of Eu^{3+} provides the location of the Eu^{2+} ground state above the VB, the IVCT band provides the Tb^{3+} ground state below the CB. Therefore, the IVCT band energy determines the quenching energy barrier ΔE and therewith the quenching temperature T_{50}. This was already demonstrated for Tb^{3+} in transition metal element based compounds in ref. 42. In ref. 14, compounds such as SnO_2, Ga_2O_3, Lu_2O_3, and GaN with low lying conduction bands were added to the collection.

IVCT bands are $\approx$0.8 eV broad and in many compounds they tend to overlap partly with the host excitation band. This introduces often larger errors in the derived value for the IVCT energy $E^{IVCT}(Tb^{3+})$. To improve accuracy, one may construct a VRBE diagram as shown in Fig. 3 that combines the spectroscopic data on many different lanthanides thus leading to more accurate ΔE values. This method was followed in ref. 14 and 42 where VRBE diagrams were constructed using the 2012 chemical shift model.[8] We will adopt here the same method but now using the refined chemical shift model which provides few 0.1 eV different $Tb^{4+/3+}$ CTL energies. The results are compiled in Table 3 and are shown in Fig. 5. Other than for Eu^{3+}, there is no need to correct for bandgap lowering with the increase of temperature because we assume that the Tb^{3+} levels move down with the same pace as the downward movement of the CB-bottom.

When assuming that the energy E^{IVCT} at the maximum of the IVCT band locates the Tb^{3+} ground state below the CB-bottom, one obtains for ΔE

$$\Delta E = E^{IVCT}(Tb^{3+}) - E(^5D_4) \quad (6)$$

where $E(^5D_4)$ = 2.55 eV is the energy of the $^5D_4$ level above the ground state and the values on $E^{IVCT}(Tb^{3+})$ can be found in ref. 62.

Table 3 T_{50} data for emission from the $^5D_4$ level of Tb^{3+} in compounds against the energy difference ΔE between the $^5D_4$ level and the CB-bottom. The parameters used for the VRBE-diagram construction are provided. All energies are in eV

A	U	E^{CT}	E_V	E^{ex}	E_C	ΔE	T_{50}	Ref.
SnO_2	7.00	3.85	−7.92	3.59	−4.23	0.79	190	45
$CaSnO_3$	6.80	4.37	−8.34	4.93	−3.21	1.55	420	46
β-Ga_2O_3	6.90	4.28	−8.40	5.05	−3.15	1.80	385	47
$CaMoO_4$	7.00	4.40	−8.47	4.60	−3.70	1.32	450	48
$KLa(MoO_4)_2$	7.05	4.20	−8.29	4.60	−3.52	1.56	455	49
$KY(WO_4)_2$	7.15	4.60	−8.74	4.55	−4.03	1.18	410	50
$KLu(WO_4)_2$	7.15	4.55	−8.69	4.50	−4.03	1.18	325	51
$LaVO_4$	6.80	3.95	−7.92	4.25	−3.53	1.24	230	52
$GdVO_4$	6.84	4.05	−8.04	4.00	−3.91	0.90	140	53
$LuVO_4$	6.80	4.06	−8.03	3.85	−4.06	0.70	80	53
$LiNbO_3$	6.87	4.47	−8.47	4.62	−3.68	1.17	200	54,55
$CaNb_2O_6$	6.85	4.10	−8.10	4.75	−3.16	1.66	490	56
$YNbO_4$	6.84	4.60	−8.59	4.96	−3.43	1.38	455	56
$LiTaO_3$	6.65	4.54	−8.44	5.50	−2.70	1.87	585	55
M′-$YTaO_4$	6.78	5.10	−9.06	5.95	−2.83	1.91	750	57
C-Lu_2O_3:(C_2)	6.60	4.81	−8.69	5.90	−2.51	2.00	525	58
$Ga_{0.7}Al_{0.3}$ N	6.40	3.22	−7.01	4.05	−2.83	1.44	250	59
GaN-wurtzite	6.40	3.25	−7.03	3.48	−3.45	0.81	30	59–61

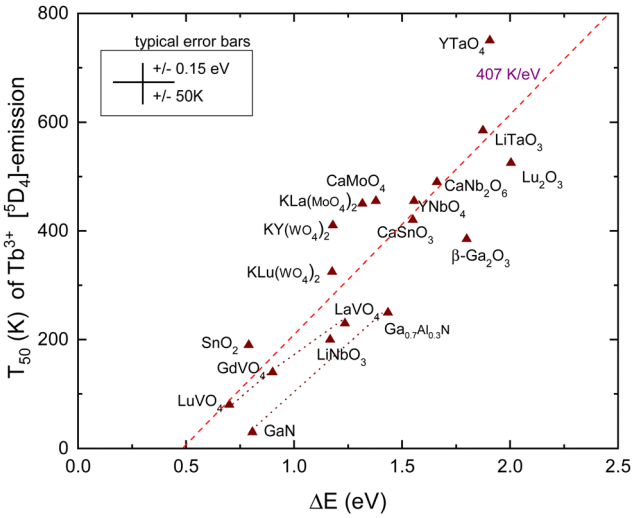

Fig. 5 T_{50} data for emission from the $^5D_4$ level of Tb^{3+} in compounds against the energy difference ΔE between the $^5D_4$ level and the CB-bottom.

When the quenching energy barrier is derived from the VRBE diagram construction one obtains for ΔE

$$\Delta E = [E^{ex} + 0.008(E^{ex})^2] - [E^{CT} - U + \Delta E(Eu, Tb) + E(^5D_4)] \quad (7)$$

where the first term between square brackets is the energy of the CB-bottom with respect to the VB-top and the second term of the $^5D_4$ state with respect to the VB-top where ΔE(Eu,Tb) $\approx$ 3.5 eV is the slightly compound dependent energy difference between the Eu^{3+} and Tb^{3+} ground state energies. The energy E^{CT} is not necessarily experimentally determined from the energy of the Eu^{3+} CT-band. It is often deduced from the constructed VRBE schemes that can be based, *e.g.*, on CT-bands other than that of Eu^{3+}, experimental IVCT energies, or photoelectron spectroscopy data.

The dashed line in Fig. 5 is from a linear least squares fit through the data and has a slope of 407 K eV^{-1}. This is somewhat smaller than the value of 475 K eV^{-1} predicted in Table 1. Nevertheless, a clear correspondence between the quenching temperature and the energy at the CB-bottom is evident. The situation and figure much resemble that of hole ionization in the case of Eu^{3+} as shown in Fig. 4. The similar lifetimes of 1–2 ms for Eu^{3+} and Tb^{3+} emissions result in similar slopes in the linear fits. Also, the intersection with the horizontal axis for both dopants occurs near 0.5 eV.

Note that the $^5D_3$ level of Tb^{3+} is located 0.7 eV above the $^5D_4$ level and therefore located 0.7 eV closer to the CB-bottom. Since the $^5D_3$ and $^5D_4$ lifetimes differ not too much (factor of 2), one may expect about 350 K lower thermal stability of the $^5D_3$ emission. Indeed, the difference amounts 375 K for $CaMoO_4$[63] and 370 K for $CaNb_2O_6$.[56] Furthermore, whenever T_{50} ($^5D_4$) is < 300 K, the emission from $^4D_3$ is absent even down to 4 K. This can be verified with the data compiled in ref. 42.

C. Thermal quenching of the Pr^{3+} $^3P_0$ emission

The $Pr^{4+/3+}$ CTL is near the same energy as that for $Tb^{4+/3+}$. Also, the emitting $^3P_0$ level of Pr^{3+} is near the same VRBE as that for

the $^5D_4$ level of Tb^{3+} as can be seen in the scheme for YPO_4 in Fig. 3. This means that like for Tb^{3+} thermal quenching may proceed by electron ionization to the CB in compounds with the low lying CB-bottom. Other than Tb^{3+} and Eu^{3+}, the next lower excited state ($^1D_2$) is only at ΔE_{mp} = 0.5 eV lower energy. At a sufficiently high temperature, the multi-phonon relaxation to $^1D_2$ then becomes also a possible quenching route. The radiative lifetime of the $^3P_0$ state is usually between 10 and 50 μs and is therefore shorter than those of Eu^{3+} and Tb^{3+}. This translates to a steeper $T_{50}/\Delta E$ = 560 K eV^{-1} slope as shown in Table 1. In ref. 42, a relationship between T_{50} of the $^3P_0$ emission and the energy of the IVCT band, or equivalently the energy distance from the CB-bottom, was already demonstrated. Since then, more data have become available. Here, we have re-analyzed everything with the refined chemical shift model. The results are shown in Fig. 6 and compiled in Table 4.

For the quenching energy barrier, we used the same method as for Tb^{3+}. When assuming that the energy $E^{IVCT}(Pr^{3+})$ at the maximum of the IVCT band locates the Pr^{3+} ground state below the CB-bottom one obtains for ΔE

$$\Delta E = E^{IVCT}(Pr^{3+}) - E(^3P_0) \quad (8)$$

where $E(^3P_0)$ = 2.55 eV is the energy of the $^3P_0$ level above the ground state and the values on $E^{IVCT}(Pr^{3+})$ can be found in ref. 62.

When the quenching energy barrier is derived from the VRBE construction one obtains for ΔE

$$\Delta E = [E^{ex} + 0.008(E^{ex})^2] - [E^{CT} - U + \Delta E(Eu, Pr) + E(^3P_0)] \quad (9)$$

where ΔE(Eu, Pr) ≈ 3.49 eV is the energy difference between the Eu^{3+} and Pr^{3+} ground state energies.

The dashed line drawn through the data has a slope of 560 K eV^{-1} as predicted from Table 1. It crosses the horizontal axis near 0.3 eV which compares with that for Tb^{3+} and Eu^{3+} where the crossing was near 0.5 eV. The data seem initially to follow this slope, but when T_{50} approaches 400 K many data points start to level off. The mentioned multi-phonon relaxation to the $^1D_0$ level may be responsible for this. A detailed analysis for each compound would be required to resolve this further. It is interesting to compare the results for the sequence of compounds $LaVO_4$, $GdVO_4$, and $LuVO_4$ where the bottom of the CB-band is formed by the lowest 3d-orbitals of V^{4+}.[42] In this sequence, this CB-bottom lowers by about 0.5 eV, see column 6 in Tables 3 and 4. For both the Tb^{3+} $^5D_4$ emission and the Pr^{3+} $^3P_0$ emission, this leads to increasingly lower T_{50} as seen in Fig. 5 and 6.

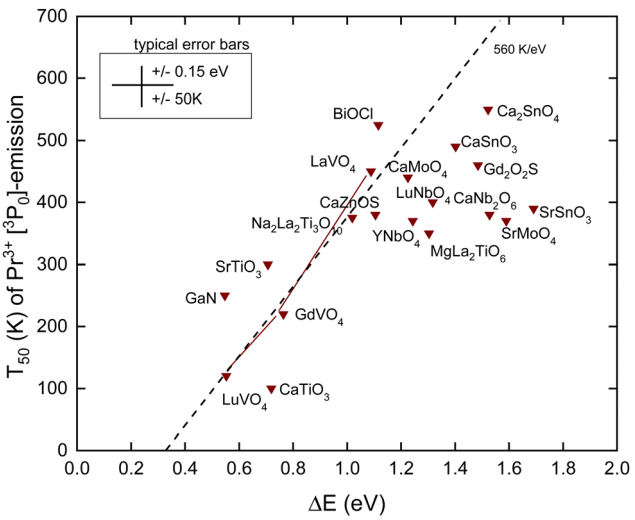

Fig. 6 T_{50} data for the emission from the $^3P_0$ level of Pr^{3+} in compounds against the energy difference ΔE between the $^3P_0$ level and the conduction band bottom.

Table 4 T_{50} data for emission from the $^3P_0$ level of Pr^{3+} in compounds against the energy difference between the $^3P_0$ level and the CB-bottom. The parameters used for the VRBE-diagram construction are provided. All energies are in eV

A	U	E^{CT}	E_V	E^{ex}	E_C	ΔE	T_{50}	Ref.
BiOCl	6.70	3.55	−7.47	4.00	−3.34	1.12	525	64
$SrSnO_3$	6.96	4.00	−8.05	4.70	−3.17	1.69	390	65
$CaSnO_3$	6.80	4.37	−8.34	4.93	−3.21	1.40	490	65
Ca_2SnO_4	6.85	4.43	−8.42	5.05	−3.17	1.52	550	65
$SrMoO_4$	7.05	4.25	−8.34	4.75	−3.41	1.59	≈370	66
$CaMoO_4$	7.00	4.40	−8.47	4.60	−3.70	1.23	440	67
$LaVO_4$	6.80	3.95	−7.92	4.25	−3.53	1.09	450	44
$GdVO_4$	6.84	4.05	−8.04	4.00	−3.91	0.76	220	53
$LuVO_4$	6.80	4.06	−8.03	3.85	−4.06	0.55	120	53
$CaNb_2O_6$	6.85	4.10	−8.10	4.75	−3.16	1.53	380	56
$YNbO_4$	6.84	4.60	−8.59	4.96	−3.43	1.24	370	56
$LuNbO_4$	6.85	4.58	−8.58	5.00	−3.38	1.32	400	68
$SrTiO_3$	6.75	3.44	−7.39	3.46	−3.83	0.71	≈300	69,70
$CaTiO_3$	6.75	3.84	−7.79	3.85	−3.82	0.72	≈100	69,70
$Na_2La_2Ti_3O_{10}$	6.75	3.70	−7.65	4.00	−3.52	1.02	375	71
$MgLa_2TiO_6$	6.68	3.88	−7.79	4.50	−3.13	1.30	350	72
CaZnOS	6.35	3.73	−7.49	4.51	−2.82	1.11	380	73
Gd_2O_2S	6.37	3.72	−7.49	4.83	−2.47	1.49	460	74
GaN-wurtzite	6.40	3.25	−7.03	3.48	−3.45	0.55	250	75,76

The $^1G_4$ level of Pr^{3+} is ΔE_{mp} = 0.86 eV below the $^1D_2$ level which makes multi-phonon relaxation from $^1D_2$ less probable than that from the $^3P_0$ level. The quenching of the $^1D_2$ emission may again proceed *via* the CB. Although the lifetime of the $^1D_2$ level is about 10 times longer than that of $^3P_0$ its 0.5 eV further distance below the CB is more important leading to the significantly higher thermal stability of the $^1D_2$ emission. The difference in T_{50} for $CaNb_2O_6$,[56] $LuNbO_4$,[68] and $MgLa_2TiO_6$[72] appears about 200 K in line with the expectation.

D. Thermal quenching of the Eu^{2+} $4f^6$ 5d–$4f^7$ emission

Techniques such as photoconductivity, excited state absorption, delayed fluorescence, and thermoluminescence charging studies have evidenced that the quenching of the Eu^{2+} emission proceeds often, if not always, by means of the thermal ionization of the 5d electron to the CB. The consistency between quenching *via* the CB and Eu^{2+} level locations with respect to the CB-bottom was demonstrated in ref. 77. The same was concluded from first principles studies on fifteen representative Eu^{2+}-doped phosphors by Jia *et al.*[78]

The nature of the 5d–4f emission is much different from that of the $4f^n$–$4f^n$ emission. The transition is dipole allowed

Table 5 T_{50} data for the Eu^{2+} 5d–4f emission in compounds (*A*) against the energy difference between the lowest energy of the relaxed $4f^6$ 5d level and the CB-bottom. The parameters used for the VRBE-diagram construction are provided. All energies are in eV

A	U	E^{CT}	E_V	E^{ex}	E_C	E_{fd}	ΔS	ΔE	T_{50}	Ref.
RbCl[a]	6.70	4.20	−8.12	7.54	−0.13	3.19	0.21	1.01	670	83
KCl[a]	6.70	4.23	−8.15	7.79	0.12	3.10	0.17	1.16	770	83
NaCl[a]	6.70	4.48	−8.40	7.96	0.06	3.02	0.12	1.15	850	83
RbBr[a]	6.60	3.10	−6.98	6.64	0.02	3.16	0.17	1.02	690	83
KBr[a]	6.60	3.53	−7.41	6.80	−0.24	3.14	0.22	1.14	717	83
NaBr[a]	6.60	3.40	−7.28	6.75	−0.16	3.02	0.13	0.96	740	83
CsI[a]	6.25	2.60	−6.31	5.80	−0.24	2.97	0.19	0.50	220	84
KI[a]	6.25	3.00	−6.71	5.88	−0.56	3.07	0.20	0.99	450	85
$Ba_5(PO_4)_3Cl$	6.89	4.40	−8.41	7.30	−0.69	3.05	0.20	0.37	510	86,87
$Sr_5(PO_4)_3Cl$	6.90	4.66	−8.68	7.50	−0.73	2.92	0.15	0.45	460	88
$Ca_5(PO_4)_3Cl$	6.88	5.04	−9.05	7.70	−0.88	2.97	0.24	0.28	480	87,89
Ca_2BO_3 Cl	6.77	4.49	−8.45	7.15	−0.89	2.68	0.43	0.60	450	90
$Ca_8Mg(SiO_4)_4Cl_2$	6.60	4.47	−8.35	6.95	−1.01	2.61	0.16	0.34	425	91
α-$Sr_2P_2O_7$	7.13	4.68	−8.81	7.85	−0.47	3.12	0.16	0.62	470	92
$LiSrPO_4$	7.05	4.77	−8.86	7.75	−0.63	2.95	0.20	0.61	450	93
$Ca_{10}K(PO_4)_7$	7.05	5.06	−9.15	8.00	−0.64	2.95	0.27	0.64	450	94
$NaCaPO_4$	7.07	4.77	−8.87	7.75	−0.64	2.77	0.31	0.85	600	95,96
YPO_4	7.09	5.65	−9.77	8.55	−0.63	2.94	0.04	0.57	230	97
$LuPO_4$	7.08	5.74	−9.85	8.70	−0.55	2.94	0.05	0.65	230	97
BaB_8O_{13}	7.30	5.15	−9.38	8.15	−0.69	3.35	0.24	0.30	500	98,99
SrB_6O_{10}	7.31	5.49	−9.71	8.30	−0.86	3.35	0.15	0.08	300	100
$Ba_2Ca(BO_3)_2$	6.93	4.61	−8.64	6.90	−1.36	2.79	0.38	0.07	190	101
$NaBa_4(BO_3)_3$	6.84	4.58	−8.57	7.00	−1.18	2.64	0.35	0.35	280	102
$NaSr_4(BO_3)_3$	6.85	4.65	−8.64	7.20	−1.03	2.67	0.69	0.64	370	102
$BaBPO_5$	7.24	4.81	−9.00	8.53	0.12	3.42	0.16	0.97	565	103
$SrBPO_5$	7.22	4.96	−9.14	8.53	−0.03	3.49	0.29	0.80	450	103
α-$CaAl_2B_2O_7$	7.03	4.96	−9.04	7.30	−1.32	3.06	0.18	−0.21	60	104
$CaBPO_5$	7.22	5.06	−9.24	8.55	−0.11	3.31	0.23	0.88	265	103
α-$SrSiO_3$	6.63	5.04	−8.93	7.70	−0.76	3.02	0.21	0.21	130	105
$CaMgSi_2O_6$	7.03	5.10	−9.18	7.95	−0.73	2.97	0.20	0.49	390	106
$Ba_2MgSi_2O_7$	6.95	4.34	−8.38	7.00	−0.99	2.84	0.37	0.40	460	107,108
$Sr_2MgSi_2O_7$	7.03	4.75	−8.83	7.29	−1.12	2.82	0.19	0.24	250	109,110
$BaCa_2Mg(SiO_4)_2$	6.90	4.20	−8.22	7.85	0.12	3.31	0.42	1.05	530	111,112
Ba_2SiO_4	6.87	4.35	−8.36	7.05	−0.91	2.70	0.24	0.52	420	113–115
Sr_3 $Mg(SiO_4)_2$	6.91	4.54	−8.57	7.45	−0.67	3.02	0.32	0.49	515	116
Sr_2SiO_4	6.81	4.64	−8.61	7.20	−1.00	3.19	0.55	0.07	425	117
Li_2SrSiO_4	6.91	4.81	−8.83	7.12	−1.30	2.43	0.26	0.42	525	118
$CaAl_2(SiO_4)_2$	6.95	4.44	−8.48	7.50	−0.53	3.08	0.19	0.53	480	119
$Ca_3Mg(SiO_4)_2$	6.86	4.96	−8.96	7.60	−0.90	3.02	0.41	0.28	435	116,120
β-Ca_2SiO_4	6.80	4.77	−8.74	7.25	−1.07	2.86	0.41	0.24	390	107
Li_2CaSiO_4	6.92	4.77	−8.80	7.55	−0.79	2.73	0.14	0.58	450	121
Sr_3SiO_5	6.74	4.07	−8.01	6.50	−1.17	2.43	0.29	0.48	485	122
$BaAl_2O_4$	6.82	4.63	−8.61	7.20	−1.00	2.92	0.44	0.29	270	123,124
$Sr_2Al(AlSiO_7)$	6.82	4.79	−8.77	7.50	−0.82	2.88	0.23	0.39	300	125
$SrAl_{12}O_{19}$	7.06	4.75	−8.85	8.00	−0.33	3.54	0.43	0.43	375	126
$SrAl_4O_7$	6.89	5.02	−9.03	8.00	−0.52	3.10	0.47	0.63	260	126
$SrAl_2O_4$:(site 2)	6.80	4.55	−8.52	6.85	−1.30	3.06	0.28	−0.25	210	127,128
$SrAl_2O_4$:(site 3)	6.80	4.19	−8.16	6.85	−0.94	2.76	0.37	0.46	420	127,128
$Sr_4Al_{14}O_{25}$:[HE-site]	7.10	4.77	−8.89	7.70	−0.72	3.49	0.44	0.13	400	129
$Sr_4Al_{14}O_{25}$:[LE-site]	6.85	4.77	−8.77	7.70	−0.59	2.82	0.30	0.73	380	129
$Ca_2Al(AlSiO_7)$	6.83	4.98	−8.97	7.60	−0.90	2.58	0.24	0.62	340	130,131
$CaAl_2O_4$	6.80	4.73	−8.70	7.40	−0.86	3.14	0.32	0.13	320	132,133
CaO	6.31	4.88	−8.62	6.94	−1.30	1.89	0.21	0.66	250	134
Ca_2SiS_4	6.40	2.06	−5.84	5.00	−0.64	2.38	0.18	0.85	445	135
$SrGa_2S_4$	6.30	1.87	−5.61	4.77	−0.65	2.55	0.23	0.65	470	136,137
$CaGa_2S_4$	6.25	1.90	−5.61	4.52	−0.93	2.36	0.14	0.49	450	138
CaS	6.17	2.35	−6.03	4.70	−1.15	2.07	0.16	0.54	475	139
$SrSi_2O_2N_2$	6.70	3.44	−7.36	6.35	−0.69	2.51	0.21	0.83	600	81
$SrSi_2AlO_2N_3$	6.60	2.97	−6.85	5.60	−0.99	2.73	0.23	0.27	450	140
$CaSi_2O_2N_2$	6.70	3.10	−7.02	6.30	−0.41	2.56	0.33	1.13	455	81
$Sr_2Si_5N_8$	6.33	2.56	−6.31	5.00	−1.11	2.19	0.18	0.53	550	141
$Ca_2Si_5N_8$	6.35	2.93	−6.69	5.15	−1.33	2.27	0.21	0.26	370	142
$CaAlSiN_3$	6.22	2.64	−6.34	5.05	−1.09	2.14	0.23	0.59	640	143,144
$SrMg_2Al_2N_4$	6.15	2.21	−5.88	4.10	−1.64	2.13	0.12	−0.05	290	145

[a] For the alkaline halides, the spectroscopic data on E^{CT} are not available. The values listed are the energy differences between the $Eu^{3+/2+}$ CTLs and E_V that was obtained directly from the published photoelectron spectroscopy data.

leading to much shorter radiative lifetimes. It varies for Eu^{2+} between 500 and 1500 ns[79] and from eqn (3) we then expect T_{50} to change with about 690 K eV^{-1}, see Table 1. A large amount of data on Eu spectroscopy have been compiled and many VRBE schemes like that of YPO_4 in Fig. 3 have been constructed. These VRBE schemes provide us with information on the energy difference between the lowest energy $4f^{n-1}5d$-level and the CB-bottom. However, there are multiple error sources in this method. We need the energy E^{CT} of the Eu^{3+} CT-band to locate the VB-top below the $Eu^{3+/2+}$ CTL. Next, we need the (estimated) energy E^{ex} for the host exciton creation to estimate the CB-bottom above the VB-top. Finally, we need the energy E_{fd} of the transition from the Eu^{2+} ground state to the lowest level of the $4f^65d$ excited state. Each step may contribute to the uncertainty in the 5d to CB-bottom energy difference. Different from the $4f^n$–$4f^n$ emissions of Eu^{3+}, Tb^{3+}, and Pr^{3+} where the Stokes shift is negligible, we have to deal with the Stokes shift ΔS between 4f–5d absorption and the 5d–4f emission that may amount 0.15 eV to almost 1 eV.[80]

The T_{50} with eqn (1) and (2) should theoretically be the same. However, quite often, the quenching of the decay time occurs at a higher temperature than that of the intensity as is the case for Eu^{2+} in $MSi_2O_2N_2$ (M = Ca, Sr, and Ba).[81] Depending on the size of the Stokes shift, the emission band overlaps partly with the absorption bands which leads to the phenomenon of self-absorption. A photon emitted by one Eu^{2+} can be absorbed by another and then again be re-emitted. As a consequence, the decay time lengthens which increases T_{50},[82] but since the luminescence quantum efficiency will be smaller than unity, the intensity decreases which lowers T_{50}. The difference between decay derived T_{50} and intensity derived T_{50} may amount 100 K. In these cases, we used an average value for T_{50}. The data on T_{50} are compiled in Table 5 together with the parameters used for the VRBE construction and ΔS.

As illustrated in the configurational diagram of Fig. 1, the excited state, after lattice relaxation, is lowered by $0.5\Delta S$ and the emission ends (arrow b) at $0.5\Delta S$ above the relaxed ground state leading to the overall Stokes shift ΔS. It is not established yet how the lattice relaxation affects the VRBE in the 5d-state but we assumed that $0.5\Delta S$ is also a measure for the lowering in the VRBE. A correction of $0.5\Delta S$ was made to obtain ΔE values in Table 5. Only the references for the quenching temperature are provided.

The used expression for ΔE is therefore

$$\Delta E = [E^{ex} + 0.008(E^{ex})^2] - [E^{CT} + E_{fd}^{Eu} - 0.5\Delta S] \quad (10)$$

where E_{fd}^{Eu} are compiled in Table 5. Note that the above equation does not contain the U-value.

Fig. 7 shows all the data on T_{50} for the Eu^{2+} 5d–4f emission derived from the luminescence intensity or decay time quenching. The dashed line through the data was constructed with a predicted slope of 690 K eV^{-1} in Table 1. The first inspection reveals a scattered collection of data where T_{50} shows a tendency to increase with ΔE. However, a least square fitted line through the data has a slope of 310 K eV^{-1} which is much smaller than the anticipated 690 K eV^{-1} value. Even when the outlier data points for $CaSi_2O_2N_2$, $SrAl_2O_4$, and $CaBPO_5$ are ignored still, a too low slope of 360 K eV^{-1} is obtained.

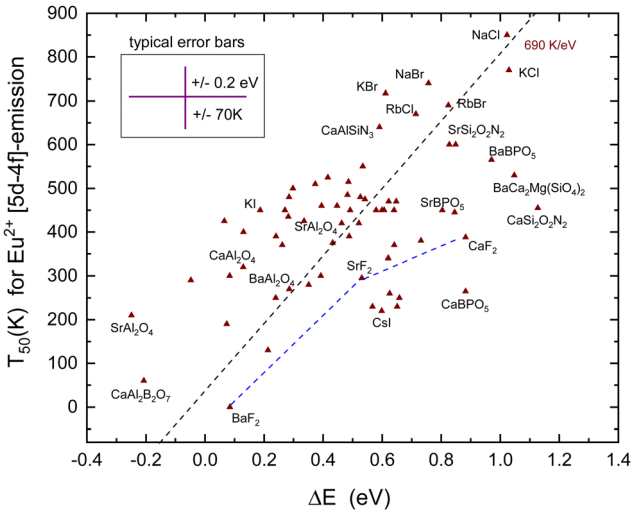

Fig. 7 T_{50} quenching data of the Eu^{2+} 5d–4f emission against the energy difference ΔE between the relaxed 5d-state and the CB-bottom. Data points for MF_2 (M = Ba, Sr, Ca) compounds are connected by straight line segments. The typical error bars are shown.

Considering all error sources, the large scatter in data is not unexpected. In constructing VRBE schemes, it is always assumed that the energy at the maximum of the Eu^{3+} CT band locates the VB-top below the $Eu^{3+/2+}$ CTL.[41] However, it is not guaranteed that this applies to the entire family of inorganic compounds. Perhaps for oxides the assumption works quite well, whereas for wide band gap fluorides or small band gap sulfides the assumption may lead to a systematic overestimation or under-estimation of the VB to the CTL energy difference which will reflect in the derived value for ΔE. The under- or over-estimation can be at most few 0.1 eV; otherwise, E_V will not be consistent anymore with the values derived from alternative methods such as photoelectron spectroscopy, computational methods, and electrochemical methods. Actually, for various small band gap compounds, the VRBE scheme places the lowest 5d-level above E_C leading to the negative ΔE. Yet, 5d–4f luminescence is observed. This may indicate that for small band compounds the CT-maximum overestimates the genuine Eu^{2+} to the VB energy difference. At this stage, it is, however, too early to enter further into this matter.

Despite the large scatter in data points, the results in Fig. 7 are consistent with the methods of the VRBE diagram construction and the errors therein. Note that almost all compounds in Table 5 concern Eu^{2+} on monovalent or divalent cation sites with the CB VRBE around or above −1 eV. Compounds with trivalent or higher valent cation sites for Eu^{2+} usually show a lower VRBE at the CB-bottom as can be verified for the compounds in Table 2–4, and *vida infra* Table 6. With few exceptions, in all these compounds, ΔE is negative and the Eu^{2+} emission is not observed.

E. Thermal quenching of the Ce^{3+} 5d–4f emission

Fig. 3 shows that for YPO_4 the VRBE in the emitting 5d level of Ce^{3+} is about 0.6 eV below that of Eu^{2+}. This energy difference is

Table 6 T_{50} data for the Ce^{3+} 5d–4f emission in compounds (A) against the energy difference between the lowest energy of the relaxed 5d level and the CB-bottom. The parameters used for the VRBE-diagram construction are provided. All energies are in eV

A	U	E^{CT}	E_V	E^{ex}	E_C	E_{fd}	ΔS	ΔE	T_{50}	Ref.
BaF_2	7.38	7.67	−11.9	10.10	−1.02	4.25	0.19	1.01	400	146–148
SrF_2	7.32	7.90	−12.1	10.60	−0.64	4.17	0.15	1.36	490	146
CaF_2	7.31	8.21	−12.4	11.10	−0.35	4.04	0.09	1.73	620	11
LaF_3	7.51	7.43	−11.8	10.45	−0.44	4.98	0.64	1.29	450	11
$LiYF_4$	7.52	8.09	−12.4	11.00	−0.46	4.32	0.19	1.72	1025	11
$LaBr_3$	6.60	2.00	−5.87	5.40	−0.24	4.07	0.54	0.94	750	149
YI_3	6.29	1.48	−5.21	4.45	−0.60	3.07	0.60	1.14	650	150
$Sr_3(Al_2O_5)Cl_2$	6.77	4.51	−8.47	6.70	−1.41	3.70	0.75	0.51	525	151
LaOBr	6.58	4.11	−7.98	6.25	−1.41	3.47	0.43	0.28	300	152,153
GdOBr	6.56	4.24	−8.10	6.40	−1.37	3.34	0.26	0.34	450	153
LaP_3O_9	7.26	5.84	−10.0	8.45	−1.02	4.28	0.21	0.80	690	154
$LiYP_4O_{12}$	7.26	6.17	−10.4	8.63	−1.15	4.19	0.21	0.77	700	155
YPO_4	7.09	5.65	−9.77	8.55	−0.63	3.85	0.13	1.32	725	156
$Ca_9Y(PO_4)_7$	7.08	4.86	−8.97	7.40	−1.13	4.31	0.68	0.62	600	157
$Ba_2Ca(BO_3)_2$	6.90	4.61	−8.63	6.90	−1.35	3.14	0.49	1.20	550	158
$LiSr_4(BO_3)_3$	6.89	4.66	−8.67	7.04	−1.24	3.73	0.75	0.82	525	159
$Li_6Gd(BO_3)_3$	6.98	4.88	−8.94	7.10	−1.44	3.59	0.36	0.71	310	160,161
$Li_6Y(BO_3)_3$	6.98	4.98	−9.04	7.20	−1.42	3.58	0.39	0.75	440	162
$La_2Si_2O_7$	6.95	5.54	−9.58	7.45	−1.69	3.79	0.29	0.18	625	163
$Gd_2Si_2O_7$	6.64	4.92	−8.81	7.20	−1.20	3.53	0.38	0.50	520	164,165
$Lu_2Si_2O_7$	7.01	5.50	−9.57	7.30	−1.85	3.54	0.29	0.36	500	166–168
$CaAl_2(SiO_4)_2$	6.95	4.44	−8.48	7.50	−0.53	4.22	0.43	0.98	635	169
$LiYSiO_4$	6.89	5.51	−9.52	7.55	−1.52	3.55	0.44	0.57	600	170
$Ca_3Sc_2Si_3O_{12}$	6.85	5.15	−9.14	7.20	−1.53	2.77	0.34	1.24	1150	171,172
$LaBO(SiO_4)$	7.03	4.84	−8.92	7.80	−0.64	4.34	0.46	0.90	600	173
$La_5\ (SiO_4)_2BO_4O$	6.84	4.38	−8.37	6.70	−1.31	3.57	0.59	0.76	395	174
X1-Gd_2SiO_5:(Ce1)	6.85	4.90	−8.90	6.80	−1.73	3.61	0.70	0.37	350	175,176
X1-Gd_2SiO_5:(Ce2)	6.85	4.90	−8.90	6.80	−1.73	3.32	0.69	0.67	250	175,176
X2-Y_2SiO_5:(Ce1)	6.86	4.80	−8.80	6.82	−1.61	3.45	0.31	0.47	440	177,178
X2-Y_2SiO_5:(Ce2)	6.80	4.81	−8.78	6.82	−1.59	3.25	0.67	0.78	410	178
X2-Lu_2SiO_5:(Ce1)	6.83	5.15	−9.14	6.85	−1.91	3.46	0.31	0.11	350	178,179
X2-Lu_2SiO_5:(Ce2)	6.83	5.15	−9.14	6.85	−1.91	3.36	0.68	0.40	290	178,179
$Sr_3Y_2Ge_3O_{12}$	6.85	4.43	−8.43	5.96	−2.18	2.86	0.38	0.51	300	172,180
$Ca_3Y_2Ge_3O_{12}$	6.85	4.77	−8.77	6.20	−2.26	2.92	0.36	0.37	265	180
$Mg_3Y_2Ge_3O_{12}$	6.90	4.70	−8.72	6.00	−2.43	2.59	0.40	0.61	300	181
$Sr_2\ Al(AlSiO_7)$	6.82	4.79	−8.77	7.50	−0.82	3.69	0.25	0.94	500	182
$Ca_2\ Al(AlSiO_7)$	6.83	4.98	−8.97	7.60	−0.90	3.48	0.30	1.09	570	182
$Gd_3Al_5O_{12}$	6.84	5.39	−9.38	6.55	−2.49	2.64	0.42	0.43	400	183,184
$GdAlO_3$	6.75	4.75	−8.70	7.36	−0.90	4.09	0.37	0.41	345	185
$Y_4Al_2O_9$	6.75	5.19	−9.13	6.45	−2.35	3.18	0.35	−0.14	60	186
$Y_3Al_5O_{12}$	6.77	5.23	−9.19	7.10	−1.69	2.71	0.33	1.01	645	11,187,188
$Y_3Sc_2Al_3O_{12}$	6.56	5.28	−9.14	6.90	−1.86	2.86	0.48	0.44	530	189
$YAlO_3$	6.81	5.06	−9.04	8.00	−0.52	4.09	0.54	0.96	660	11,190
$LuAlO_3$	6.83	5.30	−9.29	8.35	−0.38	4.03	0.51	1.18	850	190
$Ca_2\ Ga(GaSiO_7)$	6.95	4.48	−8.52	5.85	−2.40	3.54	0.49	−0.18	450	191
$Gd_3Ga_1Al_4O_{12}$	6.84	5.37	−9.36	6.50	−2.52	2.75	0.45	0.30	405	192,193
$Gd_3Ga_2Al_3O_{12}$	6.86	5.28	−9.28	6.36	−2.59	2.81	0.47	0.21	405	192,193
$Gd_3Ga_3Al_2O_{12}$	6.86	5.21	−9.21	6.29	−2.60	2.81	0.48	0.20	310	183,194,195
$Gd_3Ga_4Al_1O_{12}$	6.88	5.00	−9.01	6.07	−2.65	2.88	0.49	0.12	150	193
$Y_3Al_4GaO_{12}$	6.77	5.21	−9.17	7.10	−1.66	2.78	0.36	0.98	605	192,196
$Y_3Al_3Ga_2O_{12}$	6.77	5.23	−9.19	6.93	−1.87	2.83	0.32	0.70	525	192,196
$Y_3Al_2Ga_3O_{12}$	6.77	5.19	−9.14	6.52	−2.28	2.85	0.39	0.30	380	192,196
$Y_3AlGa_4O_{12}$	6.80	5.12	−9.09	6.44	−2.32	2.93	0.45	0.26	275	192,196
$Y_3Ga_5O_{12}$	6.85	5.05	−9.05	6.10	−2.65	2.90	0.35	−0.01	100	197,198
$SrHfO_3$	6.62	4.40	−8.28	6.35	−1.61	4.07	0.84	−0.25	285	199
$CaHfO_3$	6.64	4.51	−8.40	6.95	−1.07	3.71	0.77	0.65	360	200
$LaLuO_3$	6.58	4.25	−8.11	6.35	−1.44	3.71	0.99	0.29	339	200
$LaScO_3$	6.66	4.20	−8.10	6.20	−1.60	3.85	0.80	0.03	255	200
$La_2Be_2O_5$	6.70	4.11	−8.03	6.28	−1.44	3.64	0.85	0.49	360	32
$GdScO_3$	6.70	4.73	−8.65	6.10	−2.25	3.59	0.74	−0.34	232	200
$CaSc_2O_4$	6.65	4.35	−8.25	6.35	−1.58	2.76	0.32	0.88	530	201,202
Y_2O_2S	6.37	3.76	−7.53	4.85	−2.49	2.68	0.65	−0.21	63	203
$CaGa_2S_4$	6.25	1.90	−5.61	4.52	−0.93	2.92	0.26	0.74	575	204
$LaSiO_2N$	6.65	3.43	−7.33	5.65	−1.42	3.50	0.32	0.29	275	205
$SrAlSi_4N_7$	6.40	2.88	−6.66	5.05	−1.41	2.80	0.42	0.69	525	206
$La_3Si_6N_{11}$	6.50	3.04	−6.87	4.60	−2.10	2.72	0.36	0.19	525	207
$LaSi_3N_5$	6.48	2.58	−6.40	4.85	−1.36	3.56	0.55	0.15	550	208

typical for almost all compounds, and such an energy difference will imply a higher quenching temperature T_{50} for Ce. The lifetime of the Ce^{3+} 5d–4f emission varies between 15 ns and 65 ns[79] which is about 25 times shorter than that of Eu^{2+}. This leads to the $T_{50}/\Delta E$ = 850 K eV^{-1} rate in Table 1.

For the study of the quenching of the Ce^{3+} 5d–4f emission, the same method as for the quenching of the Eu^{2+} emission was adopted, and the used expression for ΔE is

$$\Delta E = [E^{ex} + 0.008(E^{ex})^2] - [E^{CT} - U + \Delta E(\mathrm{Eu, Ce}) + E_{fd}^{Ce} - 0.5\Delta S] \quad (11)$$

where E_{fd} are compiled in Table 6, and where ΔE(Eu,Pr) $\approx$ 5.52 eV is the energy difference between the Eu^{3+} and Ce^{3+} ground state energies.

For Eu^{2+}, the used value for the parameter U was not of relevance for obtaining the quenching energy barrier. However, for Ce^{3+}, it will be and this adds additional uncertainty to ΔE as derived from the VRBE scheme. The T_{50} values with references and the parameters used in the VRBE construction are compiled in Table 6.

The T_{50} and derived quenching energy barriers ΔE are shown in Fig. 8. The data appear to scatter like those for Eu^{2+} obscuring a clear relationship between the quenching temperature T_{50} and the quenching energy barrier ΔE. The dashed line with a slope of 850 K eV^{-1} is the predicted relationship shown in Table 1, whereas a linear fit provides only a slope of 325 K eV^{-1}. One might argue that for thermal quenching the electron need not to reach the CB-bottom but it may quench *via* CB-derived states that are still bonded to Ce^{4+}. The VRBE is then expected between E_X and E_C leading to a lowering of ΔE. It will shift and move around the data points several 0.1 eV but the general picture remains the same.

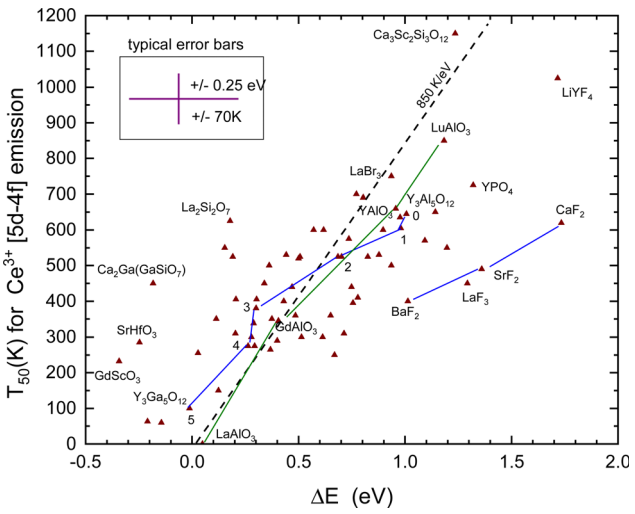

Fig. 8 T_{50} quenching data of the Ce^{3+} 5d–4f emission against the energy difference ΔE between the relaxed 5d-state and the CB-bottom. The typical error bars are shown. Data points for the sequence of compounds $Y_3Al_{5-x}Ga_xO_{12}$ and $REAlO_3$ (RE = La, Gd, Y, Lu) are connected by straight line segments.

When we deal with a sequence of similar type of compounds systematic errors will drop out yielding better correspondence with the 850 K eV^{-1} prediction. One such sequence is BaF_2, SrF_2, and CaF_2, where for both Eu^{2+} and Ce^{3+} the quenching temperature increases in accordance with the VRBE prediction. Furthermore, Ce^{3+} quenches at about 210 K higher temperature as Eu^{2+} also in accordance with the VRBE schemes. However, the data are located at about 0.5 eV too high ΔE values with respect to the data on other compounds. The reason is not known but it may indicate systematic errors in the VRBE-diagram construction. Another well-studied sequence is the Ce^{3+} doped $Y_3Al_{5-x}Ga_xO_{12}$ and $Gd_3Al_{5-x}Ga_xO_{12}$ garnet compounds. For the sequence x = 0, 1, 2, 3, 4, and 5, the data points for $Y_3Al_{5-x}Ga_xO_{12}$ in Fig. 8 have been connected with straight line segments. These data appear to follow the steeper slope of 850 K eV^{-1} much better. The same applies for the sequence $REAlO_3$ (RE = La, Gd, Y, and Lu). Ce^{3+} does not emit in $LaAlO_3$ and we assumed a ΔS = 0.4 eV to place the data point in Fig. 8. For $LuAlO_3$, we assumed $T_{50} \approx$ 850 K based on the work of ref. 190. Note that in the review work by Ueda and Tanabe[209] on Ce^{3+} doped garnet compounds the quenching data followed a slope of 620 K eV^{-1}.

Like for Eu^{2+}, there is an entire class of materials with a low lying CB-bottom and then the emitting 5d-level of Ce^{3+} is above the CB-bottom. Emission is then not observed even down to 0 K. This applies to all compounds in Tables 3 and 4.

III. Discussion

The common aspect of the luminescence quenching of all five lanthanides considered in this work is that it proceeds *via* charge carrier transfer to the CB or the VB, and the energy difference ΔE between the emitting level and the host band is the most relevant parameter. In this work, this value is derived from the constructed VRBE schemes. Table 1 shows the predicted relationship between T_{50} and ΔE where a typical value for the vibrational frequency and the luminescence lifetime was assumed. A compound to compound variation in these values is unavoidable, and this will lead to the data scatter around the predicted relationships. The data for Eu^{3+} in Fig. 4 follow the predicted slope of 435 K eV^{-1} suprisingly closely. The error in ΔE is relatively small because only the error in E^{CT} provides a dominant contribution, see eqn (5). For Tb^{3+} and Pr^{3+} in Fig. 5 and Fig. 6, ΔE is either based on the energy at the maximum of the IVCT band, see eqn (6) and (8), which usually overlaps partly with the host excitation band preventing accurate determination. The IVCT data together with the data from other lanthanides can also be used to construct VRBE schemes. Eqn (7) and (9) can then be used to determine ΔE. For both methods, the error in ΔE and the scatter in data appears larger than that for Eu^{3+}; yet, the data show consistency with the predicted slopes of 475 K eV^{-1} and 560 K eV^{-1}. For Pr^{3+}, it was suggested that above 400 K multi-phonon relaxation to the lower lying $^1D_2$ level becomes the dominant quenching route which then causes the data to deviate from the predicted trend.

Errors and resulting scatter of data become larger for the 5d–4f emitters Eu^{2+} and Ce^{3+} in Fig. 7 and 8. For Eu^{2+} errors in E^{CT}, E^{ex}, and exciton binding energy, all add to the error in E_C and therewith ΔE, see eqn (10) and (11). A standard random error of ±0.2–03 eV is estimated. In addition, there may be a systematic error related to the entire method of the VRBE construction. Particularly, the assumption that the energy at the maximum of the Eu^{3+} charge transfer band is always equal to the energy difference between the VB-top and the $Eu^{3+/2+}$ CTL might not apply for all compounds alike.[41] In a sense, the scatter of data provides insight into how accurate one can/should interpret the constructed VRBE schemes using the (refined) chemical shift model. Clearly, VRBE schemes are at this stage not accurate enough to predict the T_{50} values beforehand with a ±200 K accuracy.

To derive ΔE for Ce^{3+} requires in addition to E^{CT}, E^{ex}, and exciton binding energy also the parameter U which is a further source of error. The five outlying data points for the fluorides LaF_3, $LiYF_4$, and Ba–Sr–CaF_2 in Fig. 8 may indicate either a systematic too large value for U or that E^{CT} systematically under-estimates the $Eu^{3+/2+}$ CTL to the VB energy difference for fluoride compounds. Systematic errors are minimal when considering a series of similar compounds like the $Y_3Al_{5-x}Ga_xO_{12}$ (x = 0, 1, 2, 3, 4, and 5) or the $LnAlO_3$ (Ln = La, Gd, Y, and Lu) family. In these cases, data follow better the predicted 850 K eV^{-1} relationship as shown in Fig. 8.

The Stokes shift ΔS between the $4f^n$–$4f^n$ transitions in Eu^{3+}, Tb^{3+}, and Pr^{3+} is negligible. This is not the case for the 5d–4f transitions in Eu^{2+} and Ce^{3+} where it may amount 0.2 to above 1 eV.[80,210] One may then question how the Stokes shift will affect the value for ΔE. In deriving ΔE, we added the energy E_{fd} of the first 4f–5d excitation band to the $Eu^{3+/2+}$ and $Ce^{4+/3+}$ CTLs and subtracted 0.5 × ΔS. Following the same argumentation as for the charge transfer quenching in Eu^{3+}, Tb^{3+}, and Pr^{3+}, the 5d electron not necessarily needs to fully delocalize to the conduction band. Quenching may proceed *via* the lanthanide trapped exciton state where the electron VRBE will be somewhere between E_C and E_X. This phenomenon was used to interpret the 0.3–0.5 eV intercept of the drawn dashed lines with the horizontal for Eu^{3+}, Tb^{3+}, and Pr^{3+} in Fig. 4–6. In Fig. 7 and 8 we observe the intercept near $\Delta E \approx 0$ or even at negative values. The latter would mean that the emitting 5d-level is found inside the CB while still generating the 5d–4f emission which seems strange at least. This may indicate the limitations in the method of the VRBE construction using the chemical shift model. There may be, as noted earlier, a systematic error in the assumption that the maximum of the Eu^{3+} CT-band always defines the top of the valence band. For sure, the method of the VRBE construction does not deal with the effect of lattice relaxation. Both the Stokes shift in 4f–5d transitions and the lattice relaxation following charge transfer in the quenching phase will change level locations that can be very compound dependent. This is one of the most difficult aspects of luminescence that cannot be solved at this moment.

The difficulty in dealing with lattice relaxation and local effects can be demonstrated with the quenching of Ce^{3+} emission in oxysilicates Gd_2SiO_5, Y_2SiO_5, and Lu_2SiO_5. There are two different lanthanide sites in these compounds where Ce^{3+} is emitting at different energies. The chemical shift model assumes that the U-value is the same for both sites resulting in the site independent energy of the $Ce^{4+/3+}$ CTL. The site with the highest (E_{fd}−0.5ΔS) will have the smallest ΔE with the CB-bottom and lowest T_{50}. Yet, the opposite is observed, see Table 6. For example, the low energy emission of Ce^{3+} in Gd_2SiO_5 quenches at 100 K lower temperature than the high energy emission.[175,176] The value for U at a cation site depends on the bond lengths to the surrounding anions and on how strong anion ligands are bonded.[211,212] These are not the same for different sites in the same compound. It may well lead to few 0.1 eV difference in the U-value translating to few 0.1 eV difference in the $Ce^{4+/3+}$ CTL energy which then directly contributes to ΔE and T_{50}. We mentioned already that quenching may proceed *via* the lanthanide trapped exciton state. The VRBE in such a localized electron state is likely to be site dependent also. The message is therefore that the site dependent U-value (or $Ce^{4+/3+}$ CTL) and site dependent VRBE in the trapped exciton state are not incorporated in the general equations (10) and (11).

It is concluded that the random and systematic errors in ΔE for 5d levels as derived from VRBE schemes are generally too large to provide good predictive potential on the thermal quenching temperatures of Eu^{2+} or Ce^{3+} emission. However, in a series of related compounds, the VRBE schemes do provide the trend in the quenching temperature which can then be exploited to engineer compounds towards a better performance. Such engineering efforts are frequently performed for the garnet system of compounds. Starting with $Y_3Al_5O_{12}$ one may form a solid solution by replacing a fraction of Y for Lu or Gd, and a fraction of Al for Ga. The chemical shift model has demonstrated that the lanthanide CTLs remain fairly constant in this family of compounds. By means of solid solutions one may then change the VRBE at the CB-bottom or VB-top that translates to changing ΔE and T_{50} for the charge transfer quenching.

The above can also be demonstrated with the behavior of Tb^{3+} emission in the $Al_{1-x}Ga_xN$ solid solution.[60,61,213] From studies with Eu^{3+}, we know the energy E^{CT} and E^{ex} as a function of Ga concentration.[214] Occasionally, we also know the quenching temperature T_{10} providing data points in Fig. 4. The U-value can be estimated from that of other nitrides. Fig. 9 shows a stacked VRBE scheme of the $Al_{1-x}Ga_xN$ system with the $Eu^{3+/2+}$ and $Tb^{4+/3+}$ CTL. With the increase of the Al concentration, the VB lowers by several 0.1 eV and this leads to more stable Eu^{3+} emission as seen for the GaN (T_{10} = 200 K) and AlN (T_{10} = 300 K) data points in Fig. 4. The Tb^{3+} $^5D_4$ emission has a T_{50} of 30 K for pure GaN, but with the increase of the Al content the CB moves up and the $^5D_4$ emission stabilizes with a T_{50} of 250 K for x = 0.3. Around x = 0.5 $^5D_3$ is far enough below the CB-bottom to enable emission from the $^5D_3$ level of Tb^{3+} at 80 K although still quenched at room temperature.[59]

Horiai *et al.*[190] showed that upon replacing 20% of the Y^{3+} in $YAlO_3$ for Lu^{3+}, the T_{50} for Ce^{3+} increases from 683 K to 767 K.

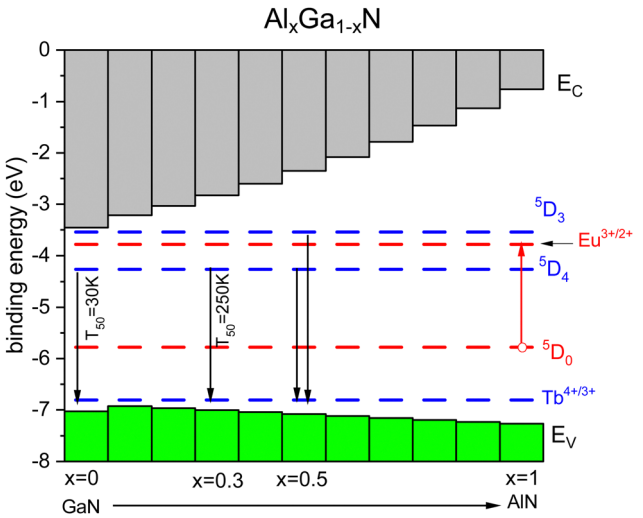

Fig. 9 Stacked VRBE scheme of the $Al_{1-x}Ga_xN$ system with the Tb^{3+} ground and excited state levels. The Eu^{3+} ground and excited $^5D_0$ levels are drawn as hole states.

With a slope relationship of 850 K eV^{-1}, 0.1 eV increase of the CB-bottom can already accomplish this increase. Lu^{3+} has a smaller ionic radius than Y^{3+}; the lattice parameters decrease and the bandgap and CB-bottom increase upon introducing Lu. Incorporating larger lanthanides such as Gd^{3+} and La^{3+} would likewise reduce the quenching temperature. Indeed, the T_{50} of $GdAlO_3$ is only 345 K and for $LaAlO_3$ there is no Ce^{3+} emission because the 5d-level is located above the CB-bottom. This is all illustrated by the corresponding data points in Fig. 8.

The sensitivity of T_{50} on slight changes in the ΔE is also well demonstrated with Ce^{3+} doped $Y_3Ga_5O_{12}$. Depending on the synthesis temperature, part of the octahedral Ga^{3+} sites can be occupied by the larger Y^{3+} cations. This is known as the anti-site occupancy which leads to slight lattice expansion and band gap narrowing. In Czochralski grown crystals the Ce^{3+} emission is absent at 10 K[197] but for powders grown with a relatively low temperature solid state synthesis there will be less anti-site occupancy, smaller lattice parameter, and wider bandgap. As a results the Ce^{3+} emission is observed at RT.[198]

Fig. 3 shows that the VRBE in the lowest 5d-state of Pr^{3+} is about 0.5 eV below that for Ce^{3+} and similar will hold for other compounds. This implies that when quenching proceeds *via* the CB, the T_{50} for the $4f^15d$–$4f^2$ emission of Pr^{3+} should be about 400 K higher than that for Ce^{3+}. For BaF_2 indeed, the 5d–4f emission from Pr^{3+} is at least 200 K more stable than from Ce^{3+}.[146] However, the T_{50} values of Ce^{3+} and Pr^{3+} in $Y_3Al_{5-x}Ga_xO_{12}$ are 640 K and 321 K for $x = 0$, 583 K and 377 K for $x = 1$, 491 K and 407 K for $x = 2$, 344 K and 316 K for $x = 3$, and 301 K and 173 K for $x = 4$.[196,215] For $x = 0$, 1, 2, 3, and 4, T_{50} (Ce) decreases because the 5d VRBE moves up and the CB-bottom moves down. However, T_{50} (Pr) increases for $x = 0$, 1, and 2 and this was attributed to quenching *via* the crossing point (CP) of the $4f^2$ [$^3P_2$] and 4f5d parabola's where the former remains stationary and the latter moves up with increasing x.[215] For $x = 3$ and 4, the CB moves down below the CP and both Ce and Pr quench *via* the CB. The question remains though why T_{50} (Pr) < T_{50} (Ce) for $x = 3$ and $x = 4$. T_{50} (Pr) < T_{50} (Ce) was also observed in Y_2SiO_5 and Lu_2SiO_5 by van der Kolk *et al.*[216] where photocurrent studies did evidence quenching *via* the CB. It was suggested that the $^1S_0$ $4f^2$ level of Pr^{3+} located above the lowest energy $4f^1$ 5d-level assists in the quenching *via* the CB thus lowering T_{50}.[216] The final answer remains open and deserves a more dedicated study.

IV. Summary and conclusions

This work confirmed that the thermal quenching of Eu^{3+}, Tb^{3+}, Pr^{3+}, Eu^{2+}, and Ce^{3+} emissions proceeds *via* charge transfer to the host band states. By using a frequency factor of 2×10^{13} Hz and the typical value for the radiative lifetime of the emitting energy level, the rate of change in T_{50} with a quenching energy barrier ΔE was predicted as shown in Table 1. Using the refined chemical shift model for the VRBE diagram construction, the ΔE values of thermal quenching were derived. For the characteristic $4f^n$–$4f^n$ emissions of Eu^{3+}, Tb^{3+}, and Pr^{3+}, the predicted slopes $T_{50}/\Delta E$ (K eV^{-1}) were indeed observed. The 0.3–0.5 eV intercept with the horizontal in Fig. 4–6 was attributed partly to the relaxation energy accompanying the charge transfer and to the possibility/probability of quenching *via* the impurity trapped exciton state. The effect of relaxation is very compound dependent and is not accounted for in the VRBE diagram construction. When the quenching temperature is above 400 K for Pr^{3+}, it was suggested that multi-phonon relaxation from $^3P_0$ to $^1D_0$ becomes a dominating route for quenching.

The ΔE values for the 5d–4f emissions of Eu^{2+} and Ce^{3+} derived from VRBE diagrams carry substantial larger errors than those for Eu^{3+}, Tb^{3+}, and Pr^{3+}. This is due to the contribution from the error in E^{ex}, the Stokes ΔS and for Ce^{3+} also the *U*-value. These error sources are held responsible for the wide scatter of the the data points in Fig. 7 and 8. Nevertheless, clear trends are observed particularly when dealing with a sequence of a similar type of compounds like the garnet or rare earth perovskite family of compounds.

This work deals with about 170 different compounds, and for each of them all parameters needed to construct VRBE schemes like that for YPO_4 in Fig. 3 have been provided in various tables. This work has demonstrated that changes as small as 0.1 eV in level locations may already lead to a 50–100 K shift in T_{50}. Such changes can be accomplished by intentional or unintentional defects, the activator concentration, the occupation of anti-sites in garnets, and the application of pressure, synthesis conditions, *etc.* As a result, the often made assumption that ΔE in the Arrhenius equations is a constant will not hold for charge transfer quenching and then there is not much scientific sense in fitting a quenching curve with this Arrhenius equation. This work has also demonstrated the limitations of VRBE diagrams as shown in Fig. 3. (1) They do not deal with lattice relaxation effects leading to the very compound dependent Stokes shifts. (2) The assumption that the maximum of the

Eu^{3+} charge transfer band always defines the energy difference between the $Eu^{3+/2+}$ CTL and the VB-top may not hold for all types of compounds. One may not exclude a few 0.1 eV differences between fluorides, oxides, and sulfides leading to systematic errors in level locations and ΔE. (3) For compounds with different sites for the activator, the same *U*-value is always used. A few 0.1 eV differences between different sites cannot be excluded, and there are indications of such differences. (4) The used *U*-values are not rigorously based on experimental or theoretical evidence and may still carry substantial errors. Despite all the above limitations, consistency between the quenching data and VRBE diagrams has been demonstrated. With a more dedicated study one might then use the quenching data as a means to further improve the method of the VRBE-diagram construction and therewith its accuracy and predictive potential.

Conflicts of interest

There are no conflicts to declare.

References

1 H. Yamamoto, *Proc. SPIE*, 2010, **7598**, 759808.
2 P. Dai, X. Zhang, M. Zhou, X. Li, J. Yang, P. Sun, C. Xu and Y. Liu, *J. Am. Ceram. Soc.*, 2012, **95**, 658.
3 N. Rakov, S. A. Vieira, Q. P. S. Silva and G. S. Maciel, *Sens. Actuators, B*, 2015, **209**, 407.
4 V. Lojpur, S. Culubrk, M. Medic and M. Dramicanin, *J. Lumin.*, 2016, **170**, 467.
5 R. A. Hansel, S. K. Desai, S. W. Allison, A. L. Heyes and D. G. Walker, *J. Appl. Phys.*, 2010, **107**, 016101.
6 M. M. Gentleman and D. R. Clarke, *Surf. Coat. Technol.*, 2005, **200**, 1264.
7 M. D. Chambers and D. R. Clarke, *Annu. Rev. Mater. Res.*, 2009, **39**, 325.
8 P. Dorenbos, *Phys. Rev. B: Condens. Matter Mater. Phys.*, 2012, **85**, 165107.
9 P. Dorenbos, *J. Lumin.*, 2019, **214**, 116536.
10 P. Dorenbos, *J. Lumin.*, 2020, **222**, 117164.
11 L.-J. Lyu and D. S. Hamilton, *J. Lumin.*, 1991, **48–49**, 251.
12 G. Gao, A. Turshatov, I. A. Howard, D. Busko, R. Joseph, D. Hudry and B. S. Richards, *Adv. Sustainable Syst.*, 2017, **1**, 1600033.
13 P. Dorenbos, *Opt. Mater.*, 2017, **69**, 8.
14 P. Dorenbos, *J. Lumin.*, 2018, **197**, 62.
15 P. Dorenbos, *J. Lumin.*, 2005, **111**, 89.
16 G. Blasse, *J. Chem. Phys.*, 1966, **45**, 2356.
17 C. W. Struck and W. H. Fonger, *J. Lumin.*, 1970, **1–2**, 456.
18 P. Dorenbos, *J. Alloys Compd.*, 2009, **488**, 568.
19 W. H. Fonger and C. W. Struck, *J. Chem. Phys.*, 1970, **52**, 6364.
20 Y. Kitagawa, J. Ueda, K. Arai, H. Kageyama and S. Tanabe, *J. Appl. Phys.*, 2021, **129**, 183104.
21 S. W. Allison and G. T. Gillies, *Rev. Sci. Instrum.*, 1997, **68**, 2615.
22 A. R. Bugos, S. W. Allison and M. R. Cates, *IEEE Proceeding Southeastcon*, 1991, 1141.
23 G. Blasse and J. de Vries, *J. Electrochem. Soc.: Sol. State Sci.*, 1967, **114**, 875.
24 E. P. Riedel, *J. Lumin.*, 1970, **1**(2), 176.
25 M. D. Chambers, P. A. Rousseve and D. R. Clarke, *Surf. Coat. Technol.*, 2008, **203**, 461.
26 G. Blasse, A. Bril and J. A. de Poorter, *J. Chem. Phys.*, 1970, **53**, 4450.
27 H. Zhu, M. Fang, Z. Huan, Y. Liu, K. Chen, X. Min, Y. Mao and M. Wang, *J. Lumin.*, 2016, **172**, 180.
28 B. Bondzior, D. Stefanska, T. H. Q. Vu, N. Miniajluk-Gawel and P. J. Deren, *J. Alloys and Comp.*, 2021, **852**, 157074.
29 S. J. Park, J. Y. Kim, J. H. Yim, N. Y. Kim, C. H. Lee, S. J. Yang and H. K. Yang, *J. Alloys and Comp.*, 2018, **741**, 246.
30 R. J. L. Steenbakker, R. G. Wellman, J. R. Nicholls and J. P. Feist, Proc. of ASME Turbo Expo 2008: Power for Land Sea and Air GT2008, June 9–13, 2008, Berlin, Germany, GT2008-51192.
31 K. S. Desai, R. A. Hansel, R. W. Pitz and D. G. Walker, 48th AIAA Aerospace Sciences Meeting Including the New Horizons Forum and Aerospace Exposition, 4–7 January 2010, Orlando, Florida, AIAA 2010-672.
32 I. N. Ogorodnikov and V. A. Pustavarov, *J. Lumin.*, 2015, **162**, 50.
33 G. A. West and N. S. Clements, *J. Lumin.*, 1992, **54**, 245.
34 S. D. Alaruri, A. J. Brewington, M. A. Thomas and J. A. Miller, *IEEE Trans. Instrum. and Meas.*, 1993, **42**, 735.
35 J. Bang, B. Abrams and P. H. Holloway, *J. Appl. Phys.*, 2003, **94**, 7091.
36 V. Jary, L. Havlak, J. Barta, M. Buryi, E. M. M. Rejman, V. Laguta and M. Nikl, *Materials*, 2015, **8**, 6978.
37 Y. Kitagawa, J. Ueda, M. G. Brik and S. Tanabe, *Opt. Mater.*, 2018, **83**, 111.
38 A. Wakahara, *Opt. Mater.*, 2006, **28**, 731.
39 T. Andreev, N. Quang Liem, Y. Hori, M. Tanaka, O. Oda, D. Le Si Dang and B. Daudin, *Phys. Rev. B: Condens. Matter Mater. Phys.*, 2006, **73**, 195203.
40 C.-W. Lee, H. O. Everitt, D. S. Lee, A. J. Steckl and J. M. Zavada, *J. Appl. Phys.*, 2004, **95**, 7717.
41 P. Dorenbos, *J. Phys.: Condens. Matter*, 2003, **15**, 8417.
42 P. Dorenbos and E. G. Rogers, *ECS J. Solid State Sci. Technol.*, 2014, **3**, R150.
43 P. Boutinaud, R. Mahiou, E. Cavalli and M. Bettinelli, *Chem. Phys. Lett.*, 2006, **418**, 185.
44 P. Boutinaud, P. Putaj, R. Mahiou, E. Cavalli and A. Speghini, *Spectrosc. Lett.*, 2007, **40**, 209.
45 D. F. Grabtree, *J. Phys. D: Appl. Phys.*, 1975, **8**, 2097.
46 Z. Liang, J. Zhang, J. Sun, X. Li, L. Cheng, H. Zhong, S. Fu, Y. Tian and B. Chen, *Phys. B*, 2013, **412**, 36.
47 Y. Tokida and S. Adachi, *ECS J. Solid State Sci. Technol.*, 2014, **3**, R100.
48 E. Cavalli, P. Boutinaud, R. Mahiou, M. Bettinelli and P. Dorenbos, *Inorg. Chem.*, 2010, **49**, 4916.

49 E. Cavalli, P. Boutinaud, T. Cucchietti and M. Bettinelli, *Opt. Mater.*, 2009, **31**, 470.
50 S. Schwung, D. Rytz, B. Heying, U. C. Rodewald, O. Niehaus, D. Enseling, T. Justel and R. Pottgen, *J. Lumin.*, 2015, **166**, 289.
51 P. Boutinaud, M. Bettinelli and F. Diaz, *Opt. Mater.*, 2010, **32**, 1659.
52 A. H. Krumpel, E. van der Kolk, P. Dorenbos, P. Boutinaud, E. Cavalli and M. Bettinelli, *Mater. Sci. Eng., B*, 2008, **146**, 114.
53 A. H. Krumpel, E. van der Kolk, E. Cavalli, P. Boutinaud, M. Bettinelli and P. Dorenbos, *J. Phys.: Condens. Matter*, 2009, **21**, 115503.
54 W. Ryba-Romanowski, S. Golab, W. A. G. Dominiak-Dzik, M. N. Palatnikov and N. V. Sidorov, *Appl. Phys. Lett.*, 2001, **78**, 3610.
55 R. Lisiecki, B. Macalik, R. Kowalski, J. Komar and W. Ryba-Romanowski, *Crystals*, 2020, **10**, 1034.
56 P. Boutinaud, E. Cavalli and M. Bettinelli, *J. Phys.: Condens. Matter*, 2007, **19**, 386230.
57 G. Blasse and A. Bril, *J. Lumin.*, 1970, **3**, 109.
58 E. Zych and D. Kulesza, *Z. Naturforsch.*, 2014, **69b**, 165.
59 A. Wakahara, Y. Nakanishi, T. Fujiwara, A. Yoshida, T. Ohshima and T. Kamiya, *Phys. Status Solidi A*, 2005, **202**, 863.
60 Y. Nakanishi, A. Wakahara, H. Okada, A. Yoshida, T. Ohshima and H. Itoh, *Phys. Status Solidi B*, 2003, **240**, 372.
61 J. Rodrigues, M. Fialho, S. Magalhaes, M. R. Correia, L. Rino, E. Alves, A. J. Neves, K. Lorenz and T. Monteiro, *J. Lumin.*, 2016, **178**, 249.
62 P. Dorenbos, *Opt. Mater.*, 2019, **91**, 333.
63 E. Cavalli, A. Belletti, R. Mahiou and P. Boutinaud, *J. Lumin.*, 2010, **130**, 733.
64 Q. Wang, M. Xie, M. Fang, X. Wu, Y. Liu, Z. Huang, K. Xi and X. Min, *Molecules*, 2019, **24**, 1295.
65 A. Stanulis, A. Katelnikovas, M. VanBael, A. Hardy, A. Kareiva and T. Justel, *J. Lumin.*, 2016, **172**, 323.
66 L. Li, P. Yang, W. Xia, Y. Wang, F. Ling, Z. Cao, S. Jiang, G. Xiang, X. Zhou and Y. Wang, *Ceram. Int.*, 2021, **47**, 769.
67 E. Cavalli, F. Angiuli, P. Boutinaud and R. Mahiou, *J. Solid State Chem.*, 2012, **185**, 136.
68 C. Liu, F. Pan, Q. Peng, W. Zhou, R. Shi, L. Zhou, J. Zhang, J. Chen and H. Liang, *J. Phys. Chem. C*, 2016, **120**, 26044.
69 P. Boutinaud, L. Sarakha, R. Mahiou, E. Cavalli, M. Bettinelli, P. Dorenbos and R. Mahiou, *J. Phys. D: Appl. Phys.*, 2009, **42**, 045106.
70 S. Okamoto, H. Kobayashi and H. Yamamoto, *J. Appl. Phys.*, 1999, **86**, 5594.
71 Y. Wang, V. Tsiumra, Q. Peng, H. Liang, Y. Zhydachevskyy, M. Chaika, P. Dluzewski, H. Przybylinska and A. Suchocki, *J. Phys. Chem. A*, 2019, **123**, 4021.
72 R. Shi, L. Lin, P. Dorenbos and H. Liang, *J. Mater. Chem. C*, 2017, **5**, 10737.
73 X. Zhang, Q. Zhu, B. Chen, S. Wang, A. L. Rogach and F. Wang, *Adv. Photonics Research*, 2021, **2**, 2000089.
74 G. Blasse and A. Meijerink, *Inorg. Chim. Acta*, 1989, **160**, 29.
75 H. J. Lozykowski, W. M. Jadwisienczak and I. Brown, *J. Appl. Phys.*, 2000, **88**, 210.
76 Y. E. Romanyuk, L. D. Kranz and S. R. Leone, *J. Appl. Phys.*, 2008, **103**, 073104.
77 P. Dorenbos, *J. Phys.: Condens. Matter*, 2005, **17**, 8103.
78 Y. Jia, A. Miglio, S. Ponce, M. Mikami and X. Gonze, *Phys. Rev. B: Condens. Matter Mater. Phys.*, 2017, **96**, 125132.
79 P. Dorenbos, *IEEE Trans. Nucl. Sci.*, 2010, **57**, 1162.
80 P. Dorenbos, *J. Lumin.*, 2003, **104**, 239.
81 V. Bachmann, C. Ronda, O. Oeckler, W. Schnick and A. Meijerink, *Chem. Mater.*, 2009, **21**, 316.
82 W. Drozdowski and A. J. Wojtowicz, *Nucl. Instrum. Methods Phys. Res., Sect. A*, 2002, **486**, 412.
83 G. Munoz, C. de la Cruz, A. Munoz and O. J. Rubio, *J. Mater. Sci. Lett.*, 1988, **7**, 1310.
84 V. Yakovlev, L. Trefilova, A. Meleshko and N. Ovcharenko, *J. Lumin.*, 2012, **132**, 2476.
85 F. Jaque, J. A. Hernandez, H. S. Murrieta and J. O. Rubio, *J. Phys. Soc. Jpn.*, 1982, **51**, 249.
86 P. Wang, J. Mao, X. Wei, L. Qiu, B. Jiang, F. Chi, M. Yina and Y. Chen, *J. Alloys and Comp.*, 2021, **869**, 159277.
87 Y. Wei, X. Qi, H. Xiao, W. Luo, H. Yao, L. Lv, G. Li and J. Lin, *RSC. Adv.*, 2016, **6**, 43771.
88 A. Garcia, B. Latourrette and C. Fouassier, *J. Electrochem. Soc.: Sol. State Science and Techn.*, 1979, **126**, 1734.
89 J. Zheng, S. Wu, G. Chen, S. Dang, Y. Zhuang, Z. Guo, Y. Lu, Q. Cheng and C. Chen, *J. Alloys and Comp.*, 2016, **663**, 332.
90 Z. Xia, L. Liao, Z. Zhang and Y. Wang, *Mater. Res. Bull.*, 2012, **47**, 405.
91 J. Wang, M. Zhang, Q. Zhang, W. Ding and Q. Su, *Appl. Phys. B*, 2007, **87**, 249.
92 W. L. Wanmaker and J. W. ter Vrugt, *Phil. Res. Rept.*, 1967, **22**, 355.
93 G. B. Nair, H. C. Swart and S. J. Dhoble, *J. Lumin.*, 2019, **214**, 116564.
94 W.-R. Liu, Y.-C. Chiu, Y.-T. Yeh, S.-M. Jang and T.-M. Chen, *J. Electrochem. Soc.*, 2009, **156**, J169.
95 C. Qin, Y. Huang, L. Shi, G. Chen, X. Qiao and H. J. Seo, *J. Phys. D: Appl. Phys.*, 2009, **42**, 185105.
96 C. Zhao, Z. Xia and M. Li, *RSC Adv.*, 2014, **4**, 33114.
97 J. Zeler, M. Sulollari, A. Meijerink, M. Bettinelli and E. Zych, *J. Alloys Compd.*, 2020, **844**, 156096.
98 G. Blasse, A. Bril and J. de Vries, *J. Electrochem. Soc.:Sol. State Sci.*, 1968, **115**, 977.
99 Y. Xie, S. Zhang, Q. Zeng, Z. Pei and Q. Su, *J. Mater. Sci. Technol.*, 2004, **20**, 517.
100 M. Leskela, T. Koskentalo and G. Blasse, *J. Sol. St. Chem.*, 1985, **59**, 272.
101 A. Diaz and D. A. Keszler, *Chem. Mater.*, 1997, **9**, 2071.
102 J. Huang, J. Dai, D. Deng, H. Yu, Y. Li, Y. Hua, S. Zhao, C. Li and S. Xu, *RSC Adv.*, 2015, **5**, 85682.
103 G. Blasse, A. Bril and J. de Vries, *J. Inorg. Nucl. Chem.*, 1969, **31**, 568.
104 S. J. Camardello, P. J. Toscano, M. G. Brik and A. M. Srivastava, *Opt. Mater.*, 2014, **37**, 404.
105 S. H. M. Poort, H. M. Reijnhoudt, H. O. T. van der Kuip and G. Blasse, *J. Alloys Compd.*, 1996, **241**, 75.

106 F. Su, B. Lou, Y. Ou, Y. Yang, W. Zhou, C.-K. Duan and H. Liang, *J. Phys. Chem. C125*, 2021, 595.
107 G. Blasse, W. L. Wanmaker, J. W. ter Vrugt and A. Bril, *Philips Res. Rep.*, 1968, **23**, 189.
108 J. Yan, C. Liu, J. Vlieland, J. Zhou, P. Dorenbos, Y. Huang, Y. Tao and H. Liang, *J. Lumin.*, 2017, **183**, 97.
109 A. A. Setlur, A. M. Srivastava, L. Pham, M. Hannah and U. Happek, *J. Appl. Phys.*, 2008, **103**, 053513.
110 D. Jia, W. Jia and Y. Jia, *J. Appl. Phys.*, 2007, **101**, 023520.
111 D. Hou, C. Liu, X. Ding, X. Kuang, H. Liang, S. Sun, Y. Huang and Y. Tao, *J. Mater. Chem. C*, 2013, **1**, 493.
112 D. Hou, W. Chen, X. Ding, H. Liang, L. Zheng and J. Zhang, *ECS J. Solid State Sci. Technol.*, 2013, **2**, R79.
113 K. Asami, J. Ueda, K. Yasuda, K. Hongo, R. Maezono, M. G. Brik and S. Tanabe, *Opt. Mater.*, 2018, **84**, 436.
114 L. Lin, L. Ning, R. Zhou, C. Jiang, M. Peng, Y. Huang, J. Chen, Y. Huang, Y. Tao and H. Liang, *Inorg. Chem.*, 2018, **57**, 7090.
115 M. Yamaga, Y. Masui, S. Sakuta, N. Kodama and K. Kaminaga, *Phys. Rev. B: Condens. Matter Mater. Phys.*, 2005, **71**, 205102.
116 G. Blasse and A. Bril, *J. Chem. Phys.*, 1968, **48**, 217.
117 T. L. Barry, *ECS J. Solid State Sci. Technol.*, 1968, **115**, 1181.
118 S. S. B. Nasir, A. Tanaka, S. Yoshiara and A. Kato, *J. Lumin.*, 2019, **207**, 22.
119 T. J. Isaacs, *ECS J. Solid State Sci. Technol.*, 1971, **118**, 1009.
120 D. Stefanska and P. J. Deren, *Opt. Mater.*, 2018, **80**, 62.
121 J. Zhong, W. Zhao, L. Lan and J. Wang, *J. Mater. Sci.: Mater. Electron.*, 2014, **25**, 736.
122 Q. Shao, H. Lin, Y. Dong, Y. Fu, C. Liang, J. He and J. Jiang, *J. Solid State Chem.*, 2015, **225**, 72.
123 H. Aizawa, S. Komuro, T. Katsumata, S. Sato and T. Morikawa, *Thin Solid Films*, 2006, **496**, 179.
124 S. H. M. Poort, W. P. Blokpoel and G. Blasse, *Chem. Mater.*, 1995, **7**, 1547.
125 F.-C. Lu, L.-J. Bai, W. Dang, Z.-P. Yang and P. Lin, *ECS J. Solid State Sci. Technol.*, 2015, **4**, R27.
126 D. Dutczak, T. Justel, C. Ronda and A. Meijerink, *Phys. Chem. Chem. Phys.*, 2015, **17**, 15236.
127 J. Botterman, J. J. Joos and P. F. Smet, *Phys. Rev. B: Condens. Matter Mater. Phys.*, 2014, **90**, 085147.
128 J. Bierwagen, S. Yoon, N. Gartmann, B. Walfort and H. Hagemann, *Opt. Mater. Express*, 2016, **6**, 793.
129 D. Dutczak, C. Ronda, T. Justel and A. Meijerink, *J. Phys. Chem. A*, 2014, **118**, 1617.
130 Y. Luo and Z. Xia, *Opt. Mater.*, 2014, **36**, 1874.
131 T. Hu, Y. Gao, M. Molokeev, Z. Xia and Q. Zhang, *Sci. China. Mater.*, 2019, **62**, 1807.
132 G. Blasse and A. Bril, *Philips Res. Rep.*, 1968, **23**, 201.
133 C. E. Tyner and H. G. Drickamer, *J. Chem. Phys.*, 1977, **67**, 4116.
134 S. H. M. Poort, A. Meyerink and G. Blasse, *J. Phys. Chem. Sol.*, 1997, **58**, 1451.
135 P. F. Smet, N. Avci and D. Poelman, *J. Electrochem Soc.*, 2009, **156**, H243.
136 C. Chartier, C. Barthou, P. Benalloul and J. M. Frigerio, *J. Lumin.*, 2005, **111**, 147.
137 J. J. Joos, K. W. Meert, A. B. Parmentier, D. Poelman and P. F. Smet, *Opt. Mater.*, 2012, **34**, 1902.
138 P. Benalloul, C. Barthou, C. Fouassier, A. N. Georgobiani, L. S. Lepnev, Y. N. Emirov, A. N. Grutzintsev, B. G. Tagiev, O. B. Tagiev and R. B. Jabbarov, *J. Electrochem. Soc.*, 2003, **150**, G62.
139 M. Ando and Y. A. Ono, *J. Cryst. Growth*, 1992, **117**, 969.
140 V. Bachmann, A. Meijerink and C. Ronda, *J. Lumin.*, 2009, **129**, 1341.
141 R.-J. Xie, N. Hirosaki, N. Kimura, K. Sakuma and M. Mitomo, *Appl. Phys. Lett.*, 2007, **90**, 191101.
142 J. Li, B. Lei, J. Qin, Y. Liu and X. Liu, *J. Am. Ceram. Soc.*, 2013, **96**, 873.
143 J. Ueda, S. Tanabe, K. Takahashi, T. Takeda and N. Hirosaki, *Bull. Chem. Soc. Jpn.*, 2018, **91**, 173.
144 J. Tian, W. Zhuang, R. Liu, L. Wang, Y. Liu, C. Yan, G. Chen, H. Xu, M. Chen, Z. Jiang and X. Zhang, *J. Am. Ceram. Soc.*, 2019, **102**, 7336.
145 P. Pust, C. Hecht, V. Weiler, A. Locher, D. Zitnanska, S. Harm, D. Weichert, P. J. Schmidt and W. Schnick, *Chem. Mater.*, 2014, **26**, 6113.
146 R. Shendrik and E. Radzhabov, *IEEE Trans. Nucl. Sci.*, 2010, **57**, 1295.
147 P. Dorenbos, R. Visser, C. W. E. van Eijk, R. W. Hollander and H. W. den Hartog, *Nucl. Instrum. Methods*, 1991, **A310**, 236.
148 R. C. Tailor, O. H. Nestor and B. Utts, *IEEE TNS-33*, 1986, 243.
149 G. Bizarri, J. T. M. de Haas, P. Dorenbos and C. W. E. van Eijk, *Phys. Status Solidi A*, 2006, **203**, R41.
150 A. M. Srivastava, S. J. Camardello, H. A. Comanzo, M. Aycibin and U. Happek, *Opt. Mater.*, 2010, **32**, 936.
151 X. Zhang, B. Park, N. Choi, J. Kim, G. C. Kim and J. H. Yoo, *Mater. Lett.*, 2009, **63**, 700.
152 Z. Fu-Tan, C. Li-Yun and X. Xu-Rong, *ECS J. Solid State Sci. Technol.*, 1987, **134**, 3186.
153 D. M. de Leeuw, C. A. H. A. Mutsaers, H. Mulder and D. B. M. Klaasen, *ECS J. Solid State Sci. Technol.*, 1988, **135**, 1009.
154 P. Dorenbos, unpublished data.
155 T. Shalapska, G. Stryganyuka, D. Trotsc, T. Demkiv, A. Gektin, A. Voloshinovskii and P. Dorenbos, *J. Lumin.*, 2010, **130**, 1941.
156 T. Justel, P. Huppertz, W. Mayr and D. U. Wiechert, *J. Lumin.*, 2004, **106**, 225.
157 C.-H. Huang, T.-M. Chen and B.-M. Cheng, *Inorg. Chem.*, 2011, **50**, 6552.
158 H. Lin, H. Liang, Z. Tian, B. Han, J. Wang and Q. Su, *J. Phys. D: Appl. Phys.*, 2009, **42**, 165409.
159 Y. Yang, B. Lou, Y. Ou, F. Su, C.-G. Ma, C.-K. Duan, P. Dorenbos and H. Liang, *Inorg. Chem.*, 2022, **61**, 7654.
160 J. F. Chen, Y. Li, G.-L. Song, D.-M. Yao, L.-Y. Yuan, X.-J. Qi and S.-H. Wang, *J. Inorg. Mater.*, 2007, **22**(1), 25.
161 I. N. Ogorodnikov, N. E. Poryvai, I. N. Sedunova, A. V. Tolmachev and R. P. Yavetskiy, *Opt. Spectrosc.*, 2011, **110**, 266.

162 Y. Ou, W. Zhou, D. Hou, M. G. Brik, P. Dorenbos, Y. Huang and H. Liang, *RSC Adv.*, 2019, **9**, 7908.
163 Q. Wei, G. Liu, Z. Zhou, J. Wan, H. Yang and Q. Liu, *Mater. Lett.*, 2014, **126**, 178.
164 V. Jary, L. Havlak, J. Barta, E. Mihokova and M. Nikl, *IEEE Trans. Nucl. Sci.*, 2014, **61**, 385.
165 O. Sidletskiy, V. Baumer, I. Gerasymov, B. Grinyov, K. Katrunov, N. Starzhinsky, O. Tarasenko, V. Tarasov, S. Tkachenko, O. Voloshina and O. Zelenskaya, *Rad. Meas.*, 2010, **45**, 365.
166 V. Jary, M. Nikl, S. Kurosawa, Y. Shoji, E. Mihokova, A. Beitlerova, G. P. Pazzi and A. Yoshikawa, *J. Phys. Chem. C*, 2014, **118**, 26529.
167 L. Pidol, A. Kahn-Harari, B. Viana, B. Ferrand, P. Dorenbos, C. W. E. van Eijk and E. Virey, *J. Phys.: Cond. Matter.*, 2003, **15**, 2091.
168 H. Feng, D. Ding, H. Li, S. Lu, S. Pan, X. Chen and G. Ren, *J. Alloys Comp.*, 2011, **509**, 3855.
169 A. Pfahnl, *Bell Syst. Tech.*, 1963, 181.
170 R. Shi, J. Xu, G. Liu, X. Zhang, W. Zhou, F. Pan, Y. Huang, Y. Tao and H. Liang, *J. Phys. Chem. C*, 2016, **120**, 4529.
171 J. M. Herzog, D. Witkowski and D. A. Rothamer, *Meas. Sci. Technol.*, 2021, **32**, 054008.
172 S. K. Sharma, Y.-C. Lin, I. Carrasco, T. Tingberg, M. Bettinelli and M. Karlsson, *J. Mater. Chem. C*, 2018, **6**, 8923.
173 L. Zhou, W. Zhou, R. Shi, C. Liu, Y. Huang, Y. Tao and H. Liang, *J. Lumin.*, 2016, **177**, 178.
174 Z. Xia, M. S. Molokeev, W. B. Im, S. Unithrattil and Q. Liu, *J. Phys. Chem. C*, 2015, **119**, 9488.
175 H. Suzuki, T. A. Tombrello, C. L. Melcher and J. S. Schweitzer, *IEEE Trans. Nucl. Sci.*, 1994, **41**, 681.
176 K. Mori, M. Nakayama and H. Nishimura, *Phys. Rev. B: Condens. Matter Mater. Phys.*, 2003, **67**, 165206.
177 E. Mihokova, K. Vavru, M. P. Horodysky, W. Chewpraditkul, V. Jary and M. Nikl, *IEEE Trans. on Nucl. Sci.*, 2012, **59**, 2085.
178 V. Jary, M. Nikl, E. Mihokova, J. A. Mares, P. Prusa, P. Horodysky, W. Chewpraditkul and A. Beitlerova, *IEEE Trans. Nucl. Sci.*, 2012, **59**, 2079.
179 J. D. Peak, C. J. Melcher and P. D. Rack, *J. Applied Phys.*, 2011, **110**, 013511.
180 H. Luo, L. Ning, Y. Dong, A. J. J. Bos and P. Dorenbos, *J. Phys. Chem. C*, 2016, **120**, 28743.
181 T. Shimizu, J. Ueda and S. Tanabe, *Phys. Stat. Sol. C*, 2012, **12**, 2296.
182 L. Lin, R. Shi, R. Zhou, Q. Peng, C. Liu, Y. Tao, Y. Huang, P. Dorenbos and H. Liang, *Inorg. Chem.*, 2017, **56**, 12476.
183 J. M. Ogieglo, A. Katelnikovas, A. Zych, T. Justel, A. Meijerink and C. R. Ronda, *J. Phys. Chem. A*, 2013, **117**, 2479.
184 I. V. Berezovskaya, A. S. Voloshinovskii, Z. A. Khapko, O. V. Khomenko, N. P. Efryushina and V. P. Dotsenko, *Funct. Mater.*, 2021, **28**, 6.
185 E. van der Kolk, P. Dorenbos, J. T. M. de Haas and C. W. E. van Eijk, *Phys. Rev. B: Condens. Matter Mater. Phys. 71*, 2005, 045121.
186 Y. Wang, R. Hrubiak, S. Turczynski, D. A. Pawlak, M. Malinowski, D. Wlodarczyk, K. M. Kosyl, W. Paszkowicz, H. Przybylinska, A. Wittlin, A. Kaminska, Y. Zhydachevskyy, M. G. Brik, L. Li, C.-G. Ma and A. Suchocki, *Acta Mater.*, 2019, **165**, 346.
187 M. J. Weber, *Solid State Commun.*, 1973, **12**, 741.
188 J. Ueda, P. Dorenbos, A. J. J. Bos, A. Meijerink and S. Tanabe, *J. Phys. Chem. C*, 2015, **119**, 25003.
189 J. Ueda, K. Aishima and S. Tanabe, *Opt. Mater.*, 2013, **35**, 1952.
190 T. Horiai, J. Pejchal, J. Paterek, R. Kucerkova, Y. Yokota, A. Yoshikawa and M. Nikl, *Jpn. J. Appl. Phys.*, 2022, **61**, 072002.
191 M. Jiao, W. Lv, L. Wei, Q. Zhao, B. Shao and H. You, *Chem. Phys. Chem.*, 2015, **16**, 817.
192 I. Venevtsev, V. Khanin, P. Rodnyi, H. Wieczorek and C. Ronda, *IEEE Trans. Nucl. Sci.*, 2018, **65**, 2090.
193 J. M. Ogieglo, *Luminescence and energy transfer in garnet scintillators*, Thesis, University of Utrecht, 2012.
194 K. Kamada, T. Endo, K. Tsutumi, T. Yanagida, Y. Fujimoto, A. Fukabori, A. Yoshikawa, J. Pejchal and M. Nikl, *Cryst. Growth Des.*, 2011, **11**, 4484.
195 T. Lesniewski, S. Mahlik, K. Asami, J. Ueda, M. Grinberg and S. Tanabe, *Phys. Chem. Chem. Phys.*, 2018, **20**, 18380.
196 J. Ueda, P. Dorenbos, A. J. J. Bos, K. Kuroishi and S. Tanabe, *J. Mater. Chem. C*, 2015, **3**, 5642.
197 A. Wittlin, H. Przybylinska, M. Berkowski, A. Kaminska, P. Nowakowski, P. Sybilski, C.-G. Ma, M. G. Brik and A. Suchocki, *Opt. Mater. Express*, 2015, **5**, 243542.
198 X. Liu, X. Wang and W. Shun, *Phys. Status Solidi A*, 1987, **101**, K161.
199 V. Jary, E. Mihokova, M. Nikl, P. Bohacek, A. Lauria and A. Vedda, *Opt. Mater.*, 2010, **33**, 149.
200 A. A. Setlur and U. Happek, *J. Solid State Chem.*, 2010, **183**, 1127.
201 Y. Chen, K. W. Cheah and M. Gong, *J. Lumin.*, 2011, **131**, 1770.
202 Q. Zhang, H. Ni, L. Wang and F. Xiao, *ECS J. Solid State Sci. Technol.*, 2016, **5**, R34.
203 H. Luo, A. J. J. Bos and P. Dorenbos, *J. Phys. Chem. C*, 2017, **121**, 8760.
204 A. Bessiere, P. Dorenbos, C. W. E. van Eijk, E. Yamagishi, C. Hidaka and T. Takizawa, *J. Electrochem. Soc.*, 2004, **151**, H254.
205 B. Dierre, R.-J. Xie, N. Hirosaki and T. Sekiguchi, *J. Mater. Res.*, 2007, **22**, 1933.
206 L. Zhang, J. Zhang, X. Zhang, Z. Hao, H. Zhao and Y. Luo, *ACS Appl. Mater. Interfaces*, 2013, **5**, 12839.
207 T. Suehiro, N. Hirosaki and R.-J. Xie, *ACS Appl. Mater. Interfaces*, 2011, **3**, 811.
208 T. Suehiro, N. Hirosaki, R.-J. Xie and T. Sato, *Appl. Phys. Lett.*, 2009, **95**, 051903.
209 J. Ueda and S. Tanabe, *Opt. Mater.: X*, 2019, **1**, 100018.
210 P. Dorenbos, *J. Lumin.*, 2000, **91**, 155.
211 P. Dorenbos, *J. Lumin.*, 2013, **135**, 93.
212 P. Dorenbos, *J. Lumin.*, 2013, **136**, 122.
213 P. Dorenbos and E. van der Kolk, *Opt. Mater.*, 2008, **30**, 1052.
214 K. Wang, K. P. O'Donnel, B. Hourahine, R. W. Martin, I. M. Watson, K. Lorenz and E. Alves, *Phys. Rev. B: Condens. Matter Mater. Phys.*, 2009, **80**, 125206.
215 J. Ueda, A. Meijerink, P. Dorenbos, A. J. J. Bos and S. Tanabe, *Phys. Rev. B*, 2017, **95**, 014303.
216 E. van der Kolk, P. Dorenbos, C. W. E. van Eijk, S. A. Basun, G. F. Imbusch and W. M. Yen, *Phys. Rev. B: Condens. Matter Mater. Phys.*, 2005, **71**, 165120.